Tunnelling and Underground Space Technology 147 (2024) 105707

Contents lists available at ScienceDirect

Tunnelling and Underground Space Technology incorporating Trenchless Technology Research

journal homepage: www.elsevier.com/locate/tust

A multidisciplinary engineering-based approach for tunnelling strengthening with a new fibre reinforced shotcrete technology

Joaquim Barros [a,*], Hugo Costelha [b,c], David Bento [d], Nelson Brites [e], Rui Luís [f], Hugo Patrício [g], Vitor Cunha [a], Luís Bento [b,h], Tiago Miranda [a], Paulo Coelho [b,c], Miguel Azenha [a], Carlos Neves [b,c], Hamidreza Salehian [a], Gonçalo Moniz [b], Mojtaba Nematollahi [a], Abel Teixeira [b], Mahsa Taheri [a], Anton Mezhyrych [b], Emad Hosseinpour [a], Tales Correia [b], Hamid Kazemi [a], Omid Hassanshahi [a], Alireza Rashiddel [a], Briar Esmail [a]

[a] *ISISE, Dep. Civil Engineering, Minho University, Guimarães, Portugal*
[b] *School of Technology and Management, Polytechnic Institute of Leiria, Leiria, Portugal*
[c] *Institute for Systems Engineering and Computers - Coimbra (INESCC), Coimbra, Portugal*
[d] *Leirimetal, Leiria, Portugal*
[e] *Teclis, Automation Systems, Leiria, Portugal*
[f] *EPOS, Empresa Portuguesa de Obras Subterrâneas, Portugal*
[g] *Infraestruturas de Portugal, Portugal*
[h] *Institute of Systems and Robotics (ISR), Coimbra, Portugal*

ARTICLE INFO

Keywords:
Tunnel strengthening
Fibre reinforced shotcrete (FRS) mix design
Experimental characterization of FRS properties
BIM
Multiscale analysis and design
Shotcrete automation and robotization

ABSTRACT

This paper describes the relevant research activities that are being carried out on the development of a novel shotcrete technology capable of applying, autonomously and in real time, fibre reinforced shotcrete (FRS) with tailored properties regarding the optimum structural strengthening of railway tunnels (RT). This technique allows to apply fibre reinforced concrete (FRC) of strain softening (SSFRC) and strain hardening (SHFRC) according to a multi-level advanced numerical simulation that considers the relevant nonlinear features of these FRC, as well as their interaction with the surrounding soil, for an intended strengthening performance of the RT. Building information modelling (BIM) is used for assisting on the development of data files of the involved design software, integrating geometric assessment of a RT, damages from inspection and diagnosis, and the characteristics of the FRS strengthening solution. A dedicated computational tool was developed to design FRC with target properties. The preliminary experimental results on the evaluation of the relevant mechanical properties of the FRS are presented and discussed, as well as the experimental tests on the bond between FRS and current substrates found in RT. Representative numerical simulations were performed to demonstrate the structural performance of the proposed FRS-based strengthening technique. Computational tools capable of assuring, in real time, the aimed thickness of the layers forming the FRS strengthening shell were also developed. The first generation of a mechanical device for controlling the amount of fibres to be added, in real time, to the FRS mixture was conceived, built and tested. A mechanism is also being developed to improve the fibre distribution during its introduction through the mechanical device to avoid fibre balling. This work describes the relevant achievements already attained, as introduces the planned future initiatives in the scope of this project.

1. Introduction

European Union (EU) authorities have fostered the extension of the high-speed rail through legislation, due to the recognition of being the “transport mode of the future”. The railway network (RN) in Europe includes several thousand km of tunnels, the majority of which were built between the middle of the 19th and 20th centuries. A significant percentage of railway tunnels (RT) present structural and functional damages, not compatible with a safe and comfortable circulation of the new generation of trains. Despite the relatively small length of RT

---

* Corresponding author.
E-mail address: barros@civil.uminho.pt (J. Barros).

https://doi.org/10.1016/j.tust.2024.105707
Received 24 June 2023; Received in revised form 28 January 2024; Accepted 6 March 2024

comparatively to the total length of the RN, the costs and the environmental impact for building these infrastructures are huge (Infrastructure Cost Review, 2010; "HS2 Guide to Tunnelling Costs, 2015), advising for their upgrade. The strengthening of tunnel linings is frequently executed using conventional materials and techniques, such is the case of shotcrete with steel meshes, which are quite time and cost demanding, and susceptible to the occurrence of serious accidents (Liu et al., 2021; Han et al., 2021; Zhang et al., 2019). Since the 90s, the use of fibre reinforcement on the shotcrete technology (fibre reinforced shotcrete, FRS) has gradually increased in tunnel stabilization and rehabilitation, due to the potential of fibres replace steel meshes with technical and economic advantages (Bernard and Thomas, 2020). However, the available FRS technology does not allow the optimum use of FRS, and current design methodologies do not consider the soil-structure interaction in a multiscale framework, which are addressed in the research conducted in the RoboShot@FRC project, herein described. Recent research has demonstrated that hybrid fibre reinforcement (FRC with more than one type of fibres) has the potential of providing strain hardening capability to the FRC (SHFRC) with great benefits in terms of load carrying capacity and ductility of structures, mainly those of high support redundancy (Smarzewski, 2019). SHFRC is a cement-based material that, under direct tensile load, develops a tensile strength higher than the stress at crack initiation of its cementitious matrix. During the strain hardening phase, up to the localization of the tensile failure crack, this composite presents high tensile deformability and energy absorption capacity, with the formation of several microcracks (Fig. 1.1). Scientific methodologies have been proposed to determine the minimum percentage of a certain type of fibres for assuring a strain hardening character to an FRC (Rubino et al., 2023). SHFRC is being used in the structural rehabilitation and strengthening of concrete and masonry type structures with notable efficiency (Di Prisco, 2022). However, SHFRCs are relatively expensive, therefore their use must be well optimized by adopting rational and reliable design methodologies. A new FRS robotic system should be controlled for being capable of applying, layer-by-layer in the tunnel area of strengthening intervention, the types of FRS determined by a multi-scale design methodology. The potential of this FRS technology was demonstrated elsewhere (Taheri et al., 2022), by determining the optimum disposition of SHFRC and strain softening FRC (SSFRC) forming an FRS thin shell for the structural strengthening of an RT. SSFRC is a fibre reinforced concrete (FRC) that, under direct tension, beyond the deformability corresponding to the crack initiation of its cement matrix, the tensile stress decreases with the imposed tensile deformability, with the formation of one predominant crack (Fig. 1.1).

Artificial neural networks (ANN) are being used to design concrete mixes and/or to predict their compressive strength (Kasperkiewicz et al., 1995; Lai and Serra, 1997; Yeh, 1999; Yeh, 1998; Yeh, 1998), with satisfactory accuracy, having been concluded that ANN are more accurate than models based on regression analysis. Boosted by the increase in computer power and improved algorithms, many studies have reported very good results, with prediction accuracies around 98 % (Asteris et al., 2016; Malagavelli and Manalel, 2014). Recently, a web application (www.aipfrc.org) has started being developed for assisting in the mix design of FRC and FRS with aimed rheological, mechanical and durability properties (Figueiredo and Barros, 2022). This tool includes a database with information about FRC and FRS mixtures and available properties at hardened stage, mainly the residual flexural strengthening parameters proposed by Model Code 2010 (Walraven, 2013) for the characterization of the FRC in terms of toughness class, and for defining its post-cracking tensile capacity under the framework of the analysis and design of FRC structures with analytical or numerical models. RoboShot@FRC project aims also to contribute for the dynamic feeding of this database.

Commercial software based on the finite element method (FEM) has been used for the simulation of the nonlinear material behaviour of FRC structures. Smeared crack and discrete crack models (SCM and DCM, respectively) are the most implemented approaches in these computer programs (Carvalho et al., 2020; Chi et al., 2017; Zhan and Meschke, 2017; Dancygier and Berkover, 2016; Teixeira et al., 2015; Deluce et al., 2014; Cunha et al., 2012; Oliver et al., 2012; Lee et al., 2011; Swaddiwudhipong and Seow, 2006; Padmarajaiah and Ramaswamy, 2002). Most of these models consider the contribution of fibre reinforcement mechanisms through a cohesive traction-separation law obtained from semi-empirical recommendations, or from experimental results, either directly or from inverse analysis (IA) (Matos et al., 2021). For modelling an FRS shell applied with the new shotcrete technology for the structural strengthening of an RT, this curved shell should be simulated by layers, and each layer can have different properties for modelling its behaviour in serviceability and ultimate limit state conditions. The interaction of

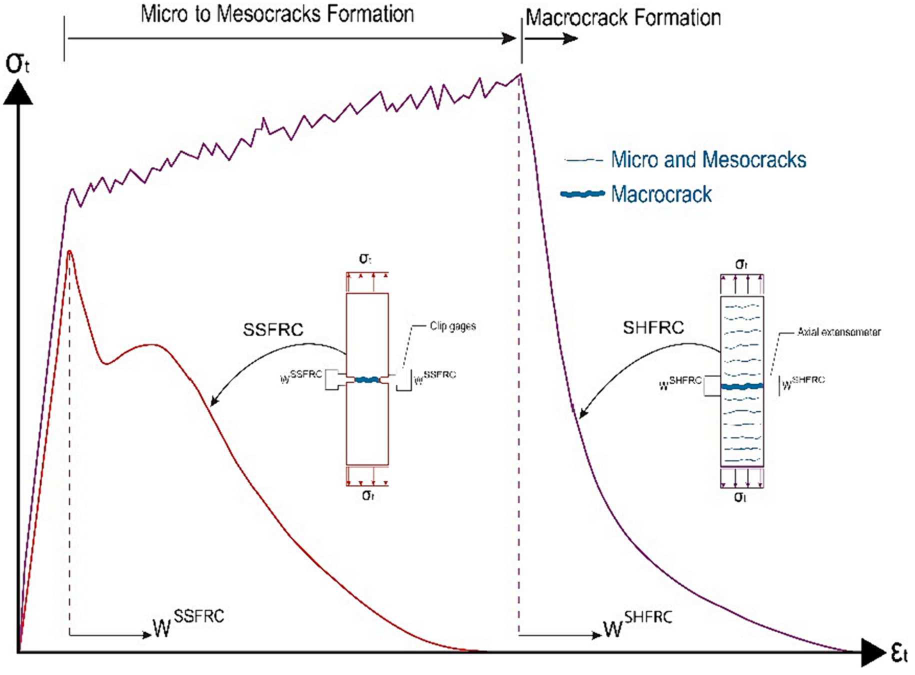

Fig. 1.1. Test recommendation and typical tensile behaviour of a strain softening and strain hardening fibre reinforced concrete.

the FRS shell with its surrounding soil should be properly simulated. FLAC^{3D} software is being used for this purpose due to the specialized constitutive models for simulating, in a comprehensive strategy, the fundamental phenomena occurring in soil and rock systems (Nematollahi and Dias, 2019; Nematollahi and Dias, 2020; Sánchez, 2019).

In the last years some advances have been done on the assessment of the tunnel's geometry, properties, and damages (Malva and Wißler, 2014). This information should be integrated with building information modelling (BIM) for the generation of twin RT, and its design according to a multiscale approach. Despite the increasing adoption of BIM in the context of buildings (Eichler et al., 2023), particularly in view of government mandates and available standards (e.g. ISO19650 series (14:00-17:00, "ISO 19650-1:2018, 2023), its adoption in tunnel infrastructure is not at all generalized yet, in view of the incapacity of Industry Foundation Classes (IFC) to directly handle tunnel entities (a project on IFCTunnel has begun in 2019 and should produce impact soon (buildingSMART, 2020). Important efforts, such as CrossRail (Taylor, 2023) and RailBaltica (Rail, 2023), have been exhibiting the possibility of using BIM in general for infrastructures with tunnels.

Specialized shotcrete equipment has been used in several applications of civil and mining engineering to minimize the shotcreting time and to increase the safety conditions of the execution procedure (Nabulsi et al., 2010) (Liu et al 2022); (Galan et al., 2019) . Most shotcrete applications involve an operator remotely controlling the equipment on site (Nabulsi et al., 2010); (Liu et al., 2022); (Cheng et al., 2001) , although for some operations the nozzle can be manually held by the operator. The shotcrete projection is applied in layers with a given thickness and concrete composition, according to a shotcrete plan, in general based on a structural design that ensures structural stability (Nabulsi et al., 2010). A skilled operator is needed to ensure a projection trajectory that leads to layers with the desired thickness, while minimizing rebound (concrete which is projected but does not adhere to the projected surface). The rebound increases with the deviation from the orthogonality to the projection direction (Malmgren et al., 2005). Automating this process can be done by recurring to robotics together with automatic path generation and control, and an adequate perception system, allowing to relieve workers from these hostile environments, while contributing to increase the quality and efficiency of the shotcreting process (Liu et al., 2022); (Girmscheid and Moser, 2001; Rodríguez and Río, 2007; Chun-Lei et al., 2020) . Although there are several developments towards this goal (Nabulsi et al., 2010); (Liu et al., 2022); (Cheng et al., 2001); (Girmscheid and Moser, 2001); (Chun-Lei et al., 2020) , and Normet, a Finnish company, has announced that it has plans to offer a fully autonomous shotcrete system, currently there is no automatic shotcrete equipment on the market (Lin et al., 2019). RoboShot@FRC aims to contribute to this development, particularly to the possibility of applying FRS with the properties required by the structural stability design. To this purpose, the robot should be able to add, in real time, the content of fibres in a premixed FRC, in order the FRS, to be applied in a certain layer/zone, has the aimed properties. The flowchart of the relevant aspects of technology proposed in this project is indicated in Fig. 1.2.

2. Assessment of the geometry and damages in tunnels and its integration in a BIM model

As responsible for its own asset management, 'Infraestruturas de Portugal (IP)' has been making inspection, monitoring, and diagnosis of RT since 1999. The process of inspection/monitoring started to be digitalized in 2004, in collaboration with SPACETEC/Germany, and by deploying several inspection techniques (Malva and Wißler, 2014) within a specially adapted vehicle, the EM120, that carries a scanning device. Right now, all the 80 railway tunnels of IP have a wealth of digitalized data that is available as input in the scope of the RoboShot@FRC framework. The data includes the laser scanning, photogrammetry and thermography of the tunnels, as well as the traditional human visual inspection and traditional inspection/monitoring techniques (permanent and non-permanent) such as: strain sensing with fibre optics, topography stations, crack monitoring, load cells, piezometers, inclinometers, corrosion sensors, endoscopy and Ground Penetrating Radar, GPR, (Inspecção, 2011). Most of the above-mentioned tunnel data is conveniently stored and analysed in a competent dedicated software for the purpose, named Tunnel-Inspector (by SPACETEC), which allows integrated data overlapping/analysis and mapping of visual inspections as overlays to the other data. Some screenshots of the data integration can be seen in Fig. 2.1.

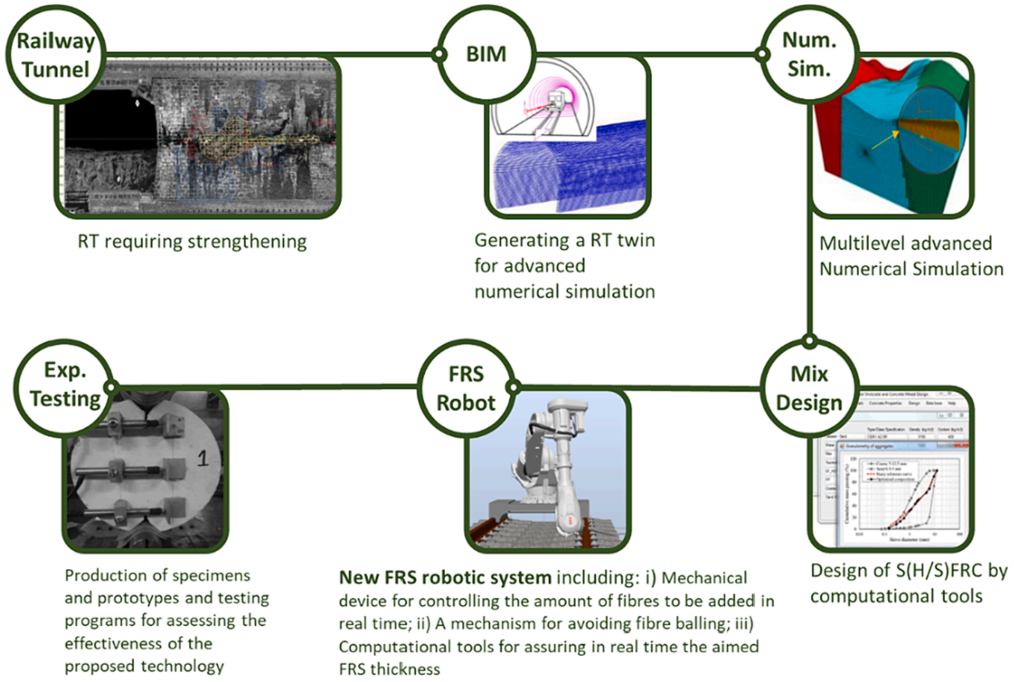

Fig. 1.2. Main characteristics of the technology proposed in the RoboShot@FRC project.

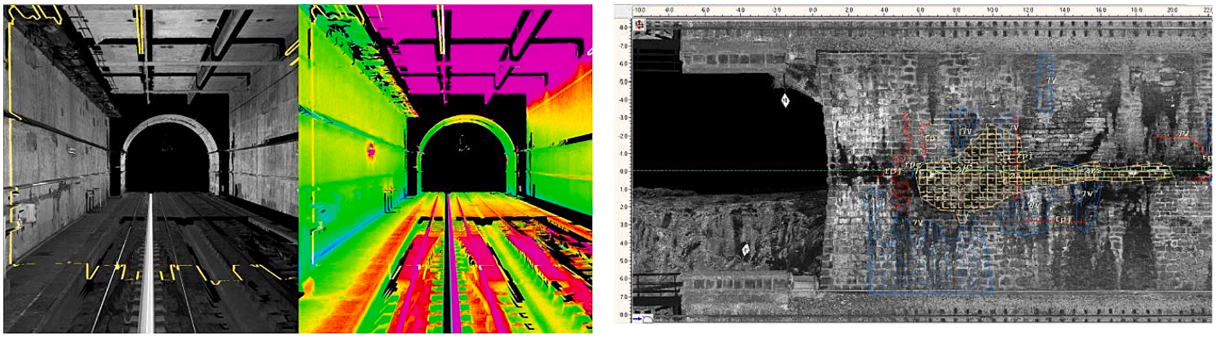

a) b)

Fig. 2.1. Examples of information gathered in the digitized tunnel inspection management: (a) overlay of layers of geometry and other data; b) visually inspected damage mapping overlay on the laser scanning and photogrammetry data.

The information needed for the work described in the following sections can be harvested from the currently existing databases, with most being retrievable from the laser scanning point clouds that allow feature extraction and establishing baselines for the 3D geometry of the surface to receive shotcrete.

The developments made so far in integration with BIM include the establishment of the modelling rules, comprising definitions of geometrical and non-geometrical information. As the model to be used pertains to the combined use of 'facility management' and 'shotcrete projection' (where applicable), the geometrical definition is generally simplified, except for the requirements regarding the surface of the tunnel lining (to support the shotcrete layer). Focus has been given mostly to non-geometrical information, where developments were necessary to define the relevant information to include. Two fundamental principles were followed: (i) always perform modelling with interoperability in mind (hence with proper export to IFC envisaged); (ii) follow a sound strategy for non-geometric data, including a "product data template, PDT" approach. The Building Information Models are being prepared in Autodesk Revit 2023, while carefully exporting information to the IFC format for legacy information. An example of a modelled tunnel is shown in Fig. 2.2a, based on a laser scan, allowing the hosting of all the necessary information for facility management coming from the existing database. Strong emphasis has also been input into the production of specifically driven 'product data templates', in accordance with ISO-CEN recommendations (EN ISO 23386:2020 and EN ISO 23387:2020 standards), and with implementation in the national Portuguese platform pdts.pt, which hosts standardized information for the entire industry nation-wide. A part of the developed data template, which paves the way for country-wide normalization in tunnels (and inspire worldwide initiatives in this field of tunnels, which are scarce), is shown in Fig. 2.2b for illustrative purposes. It is noted that the PDT for shotcrete lining is available for free in the pdts.pt platform, and that this is a live standard, constantly evolving. It is also noted that developments on other data templates of relevance for RoboShot@FRC are being developed, namely: ballast, rail, fastening system, sleeper, tunnel lining, and anomalies in tunnel lining.

3. Fibre reinforced concrete/shotcrete mix design compositions

Due to the limited number of publications with detailed data on the FRC and FRS mix compositions and their corresponding properties at fresh and hardened states, a web platform (aipfrc.org) started being developed for collecting this type of information (Figueiredo and Barros, 2022). This platform integrates machine learning (ML) algorithms to propose the optimum FRC or FRS mix composition for targeted properties at fresh and hardened states, but at the present stage is still limited to the residual flexural tensile strength parameters, f_{Rj}, proposed by Model Code 2010 (Walraven, 2013) to characterize the post-cracking tensile capacity of FRC. Since this goal is quite dependent on the size and reliability of the information collected in the database, search

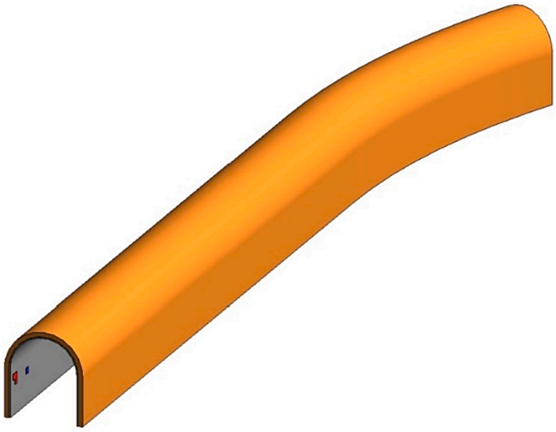

a)

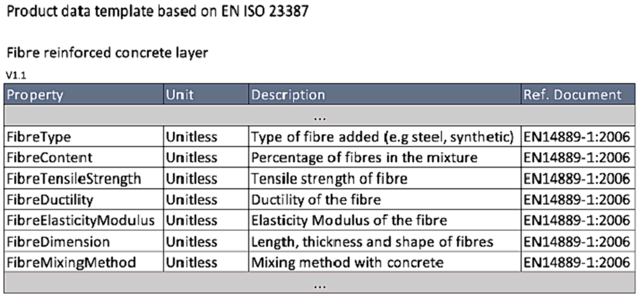

Product data template based on EN ISO 23387

Fibre reinforced concrete layer

V1.1

Property	Unit	Description	Ref. Document
…			
FibreType	Unitless	Type of fibre added (e.g steel, synthetic)	EN14889-1:2006
FibreContent	Unitless	Percentage of fibres in the mixture	EN14889-1:2006
FibreTensileStrength	Unitless	Tensile strength of fibre	EN14889-1:2006
FibreDuctility	Unitless	Ductility of the fibre	EN14889-1:2006
FibreElasticityModulus	Unitless	Elasticity Modulus of the fibre	EN14889-1:2006
FibreDimension	Unitless	Length, thickness and shape of fibres	EN14889-1:2006
FibreMixingMethod	Unitless	Mixing method with concrete	EN14889-1:2006
…			

b)

Fig. 2.2. A) example of a tunnel modelled with the intended framework; b) part of the data template for shotcrete tunnel lining.

engine tools are being developed to dynamically feed the database with data automatically extracted from papers published in WoS journals. Despite the efforts that are being done in this complex task, the collected data continues to be relatively scarce, requiring a complementary research strategy involving the development of a software for the mix design of FRC/S and the characterization of their properties in a fresh and hardened state. The Graphical User Interface (GUI) of this software, designated by FRMixD, is illustrated in Fig. 3.1.

FRMixD is based on the method developed by Faury (Faury, 1958), which is a particle-packing model (PPM). A modified version of the PPM was implemented in the FRMixD, which was also adapted to consider the influence of fibres in the optimum arrangement of the aggregates regarding the maximum compacity and internal friction angle of its skeleton. As will be detailed in Section 6, the new shotcrete technology assumes that an FRC with properties suitable for the major zone of structural strengthening intervention in an RT is supplied to the robot system, and an extra content of steel fibres is added in real time by the robot system to the FRC, in order to ensure an FRS with the properties required by the design project for the particular zone that is being shotcrete. The FRC is produced according to a ready-mix technology and can already include fibres different from the ones to be added by the robot system in the projection moment. Therefore, the FRMixD should be capable of designing not only the optimum FRC but also the final FRS. The influence of each type (material and/or geometry) and content of fibres must be properly accounted by the adapted PPM implemented in FRMixD.

The PPM includes the Faury parameters for considering the influence of the nature of the used aggregates and aimed concrete workability (Faury, 1958). These parameters were originally calibrated for plain concrete. Therefore, research on the technology of FRC/S has been conducted to determine the values of these parameters for FRC/S. The database of FRMixD allows to determine the optimum aggregate skeleton arrangement based on the available type of aggregates, and includes the properties of the FRSC/S at fresh and hardened states, synchronized with the AIpFRC to feed this platform with the information from the FRMixD.

A tunnel's formwork was built (Fig. 3.2a) for serving as a real scale laboratory, where the potential of the new shotcrete technology for accomplishing the application of the aimed FRS is assessed. The rebound is determined, and the mechanical and durability properties of the FRS are evaluated in cores extracted locally and from specimens and prototypes produced in this lab (Fig. 3.2b).

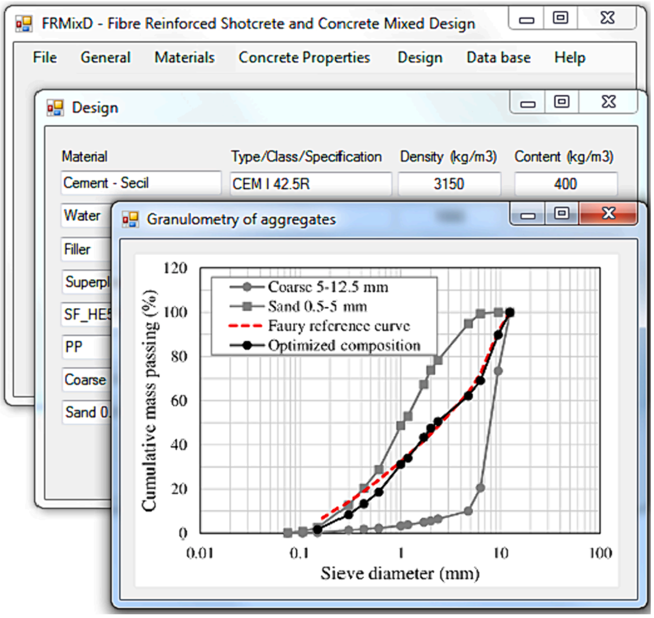

Material	Type/Class/Specification	Density (kg/m3)	Content (kg/m3)
Cement - Secil	CEM I 42.5R	3150	400
Water			
Filler			
Superpl			
SF_HE			
PP			
Coarse			
Sand 0			

Fig. 3.1. Graphical User Interface of FRMixD software.

4. Assessment of FRS properties

An extensive experimental programme is being carried out for having data correlating FRS mix compositions from the FRMixD with their properties at fresh and hardened states, as well as data for the multiscale modelling described in Section 5. The specimens used for material characterization were extracted outside the defective zone as defined by EN 14488:1 (2005) (EN, 2005), so that the assessed experimental material properties would not be influenced by wall effects, and, consequently, are representative of its behaviour on the real application.

4.1. Compressive tests

Compressive tests are executed on cores with a diameter of 50 mm and a height of 100 mm, extracted along two directions, respectively, parallel and perpendicular to the shotcreting direction, (Lnec, 1993; Cunha et al., 2008). Average values of modulus of elasticity and compressive strength for the parallel and perpendicular specimens are: 31.5 GPa and 50.5 MPa; 33.2 GPa and 43.1 MPa. Since the fibres have the tendency to orientate preferably orthogonally to the shotcreting direction, the fibres-matrix interfaces, which are weakest zones on the microstructure of this composite material, have higher detrimental effects in terms of compressive stiffness and strength when the compressive loading actuates orthogonally to the shotcrete direction. The results from the two groups of tests suggests that the compressive strength in the orthogonal to the shotcrete direction is of one strength class smaller than the compressive strength in the parallel direction.

4.2. Flexural and indirect tensile tests

The flexural behaviour is being assessed through four-point bending tests (4PBT) on 75 × 125 × 500 mm^3 prismatic specimens, according to the EN 14488-3 (2006) (EN, 2006). Additionally, the tensile behaviour is being characterized through several indirect tensile tests, such as the modified splitting tensile test (MSTT), the round panel test (RPT), and three-point bending test, on notched specimens (3PBT), (Cunha, 2010; Lameiras et al., 2015). The stress-crack width (σ-w) will be determined by performing inverse analysis (IA) with the experimental results of the RPT and 3PBT (Matos et al., 2021; Soltanzadeh et al., 2019) . The σ-w is fundamental for modelling the post-cracking tensile behaviour of FRS (described in Section 5). For deriving the σ-w in case of slabs and shell type FRC structures, it is recommended that the IA be applied to the results obtained in RPT since, in this test, the fibre distribution and orientation best reflect the cracking process on this type of FRC/S structures (Soltanzadeh et al., 2019). However, available information in this respect shows that the σ-w relationships derived from the IA provide unsafe predictions (Salehian and Barros, 2015). Another important aspect of the simulation of FRC/S structures is how to take into consideration the dispersion of results in RPT in the constitutive laws simulating the FRC/S. In fact, due to the relatively smaller fracture surface of these specimens, regarding the total fracture surface occurred in real FRC/S structures, mainly in those with high degree of static indeterminacy, the number of fibres contributing for the post-cracking tensile capacity is much smaller than in real structures, resulting in a higher coefficient of variation values in these small-scale tests (Matos et al., 2021; Soltanzadeh et al., 2019) . The σ-w obtained from IA will be compared to the one obtained directly in the MSTT to correlate this information with the fibre distribution and orientation in these types of tests, for its consideration on the constitutive models adopted to simulate the behaviour of FRS.

Fig. 4.1. and Fig. 4.2 show the typical results obtained in three-point notched beam bending tests (3PNBT) and in four-point bending tests (4PBT), respectively. These tests (the number is indicated in the caption

a)

b)

Fig. 3.2. A) tunnel's formwork serving as a shotcrete laboratory; b) production of specimens for the experimental programs.

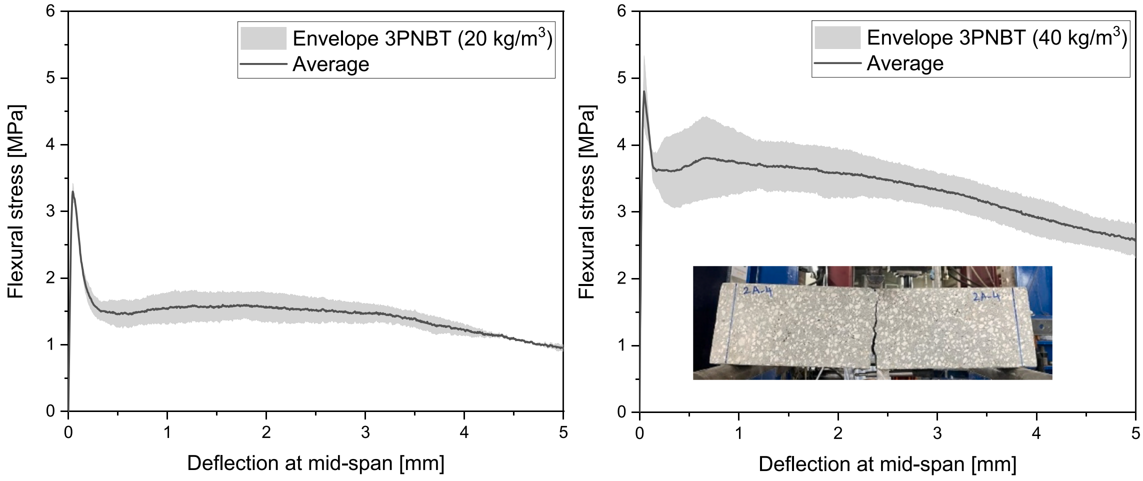

a)

b)

Fig. 4.1. Typical results of the flexural stress – deflection relationships obtained through three-point notched beam bending tests for the compositions with: (a) 20 kg/m^3 (2 specimens) and (b) 40 kg/m^3 (2 specimens).

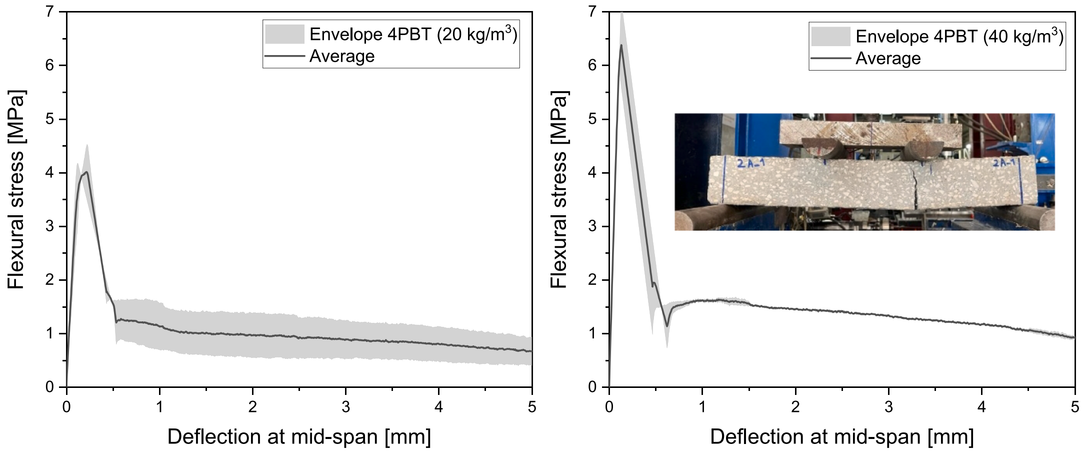

a)

b)

Fig. 4.2. Typical results of the flexural stress – deflection relationships obtained through four-point bending tests for the compositions with: (a) 20 kg/m^3 (2 specimens) and (b) 40 kg/m^3 (2 specimens).

of the figures) were executed in specimens produced with the conventional FRS technology, by using distinct mixtures of 20 and 40 kg/m^3.

The flexural behaviour of the two series of 3PNBT is according to what was expected. In fact, after crack initiation of the matrix, the higher content of fibres in the series with 40 kg/m^3 of fibres allowed a significant increase of the peak flexural capacity over the series with 20 kg/m^3 of fibres. The drop of the flexural capacity is also smaller since the notched cross section has larger number of fibres resisting to the crack opening due to pullout resisting mechanisms. The post cracking tensile capacity of a FRC, $\sigma_{FRC}(w)$, is the addition of the contribution of the matrix, $\sigma_c(w)$ plus of the pullout resisting mechanisms provided by fibres crossing the crack, $\sigma_f(w)$, as shown in Fig. 4.3.

Since the 4PBT do not have a notch, both series of 4PBT presented higher flexural strength than the corresponding series of 3PNBT. However, the post-cracking flexural capacity of both series of 4PBT was significantly smaller than the corresponding series of 3PNBT. Since a notch was not applied in the 4PBT, the flexural failure crack has initiated in the weakest section in the pure bending region of the specimen, i.e., in the section with the minimum number of fibres or/and more deficiently distributed and oriented, as shown in the photos included in Fig. 4.2. However, further inspection will be conducted on the specimens of the series of 4PBT reinforced with 40 kg/m^3 of fibres, since it was not expectable a so low post-cracking tensile capacity.

4.3. Shear and bond tests

The shear capacity of the FRS is assessed by performing direct FIP shear test (Fig. 4.4a), whose test setup is described in detail elsewhere (Salehian and Barros, 2015). The in-plane bond shear behaviour is assessed by performing experimental tests according to the setup shown in Fig. 4.4b, which is described elsewhere (Salehian and Barros, 2015). Different levels of confinement are adopted for determining its influence on the constitutive law modelling this interface. Since a major part of the old RT in Portugal has a masonry arch substrate in granitic and clay blocks, these are the two substrates adopted in the specimens of the experimental program (Fig. 4.4b and Fig. 4.4c). The influence of the level of roughness of these substrates on the bond behaviour is also investigated to determine how relevant is the pre-treatment of the substrate (i.e., hydro/sand blast) before the application of the FRS shell.

Typical results on the in-plane bond shear tests are presented in Fig. 4.5 and Fig. 4.6 for the granite and clay substrate, respectively, where the acronym adopted to nominate a specimen, XYZ_#, has the following meaning: X can assume the letter G or C to represent granitic or clay substrate, respectively; Y can be SS or RS to indicate smooth or rough surface of the substrate, respectively; Z indicates the level of confinement stress, in MPa; # is the number of the specimen in the same group of tests. For instance, GSS1.0_1 is the specimen number one of granitic substrate, with smooth surface tested under a confinement level of 1.0 MPa. From these results, it is shown that, by increasing the roughness of the substrate, the in-plane bond strength is increased, regardless the type of used substrate. The main difference from the two types of substrates is the higher residual shear strength assured by the clay substrate.

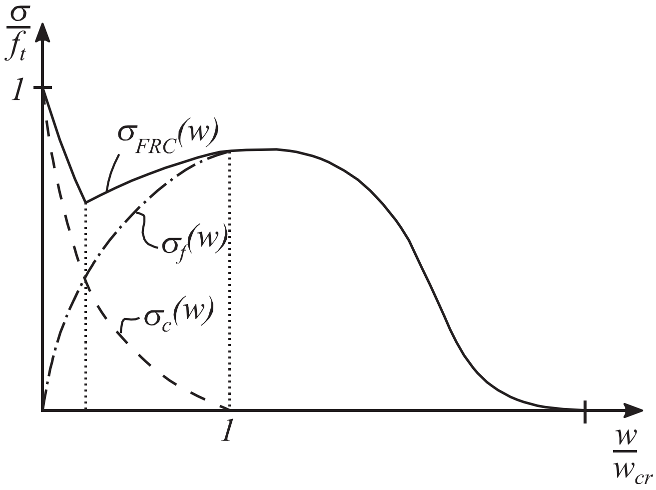

Fig. 4.3. Contribution of matrix, $\sigma_c(w)$, and fibre reinforcement, $\sigma_f(w)$, for the post-cracking tensile capacity of a FRC, $\sigma_{FRC}(w)$.

5. Integrated design of tunnel strengthening with FRS

An RT case study provided by “Infraestruturas de Portugal”, namely the Mourilhe RT, is being numerically simulated with two different software of complementary objectives in the context of the strengthening of this RT, with the innovative technology based on the application of FRS with a new robotic system, which is described in Section 6. A macro modelling was performed by FLAC^{3D} (FLAC, 2019) to determine the strain and stress field in the medium affected by the construction of the RT, as well as to define a domain for a more refined analysis with the FEMIX software (Barros, 2016), which can simulate the nonlinear behaviour of the FRS and its contact with the substrate. The relevant results are presented and discussed in the present section.

5.1. Macro modelling

From the 2D topographical map represented in Fig. 5.1a, the 2D contour lines were transferred to Civil3D software to derive their corresponding 3D contour lines (Fig. 5.1b). By using the Rhinoceros3D software, the ground surface was generated from the 3D contour lines (Fig. 5.1c), whose file in “.stl” format was imported by FLAC^{3D}. The mesh shown in Fig. 5.1d, composed of tetrahedral polygons, was then generated.

The computational model of the Mourilhe tunnel is shown in Fig. 5.2, whose dimensions were determined following the recommendations of Rodriguez (Medina-Rodríguez, 2000), regarding the minimum extension of the model in order the main conclusions of the analysis do not be affected by the boundary conditions, which are represented in Fig. 5.2a.

In the initial equilibrium analysis using the Mohr-Coulomb constitutive model with the estimated parameters corresponding to weathered granite (Table 5.1), the in-situ displacement and stress fields, existing before the excavation of the tunnel, were determined by considering the self-weight of the materials intervening on the model. The corresponding vertical (z direction) and horizontal (x direction) stress fields are represented in Fig. 5.3, where it is shown that the vertical stress is much lower than the compressive strength of the weathered granite rock.

The Mourilhe tunnel was excavated in weathered rock media according to the Belgian excavation procedure, whose numerical simulation is shown in Fig. 5.4, by considering the tunnel’s phase construction (Kargar et al., 2020).

The vertical displacement field at cross-section y = 126 m (see Fig. 5.2) is shown in Fig. 5.5, after the tunnel has been completely excavated. It is shown that the excavation had caused a final maximum deflection of 0.3 mm on the crown of the masonry lining, and 0.8 mm upward displacement in tunnel invert.

For determining the critical zone around the tunnel’s cross section, i.e., the more susceptible to structural instability, two methods were considered. In the first method, herein designated by “stepwise reduction of material properties”, the following scenarios were adopted in terms of reducing the cohesion and the internal friction angle of the soil: 1) Reducing cohesion up to 50 % in 5 steps; 2) Reducing cohesion up to 100 % in 10 steps; 3) Reducing friction angle up to 50 % in 5 steps; 4) Reducing friction angle up to 100 % in 10 steps. Fig. 5.6 shows the vertical displacement field and the maximum principal stress field at tunnel’s section y = 126 m for the scenario 2. This selected scenario was the one of highest impact on the maximum vertical and lateral

a) b) c)

Fig. 4.4. A) direct shear tests (fip) on frs specimens; b) and c) in-plane bond shear behaviour between frs and granitic (b)) and clay (c)) tunnel's substrates.

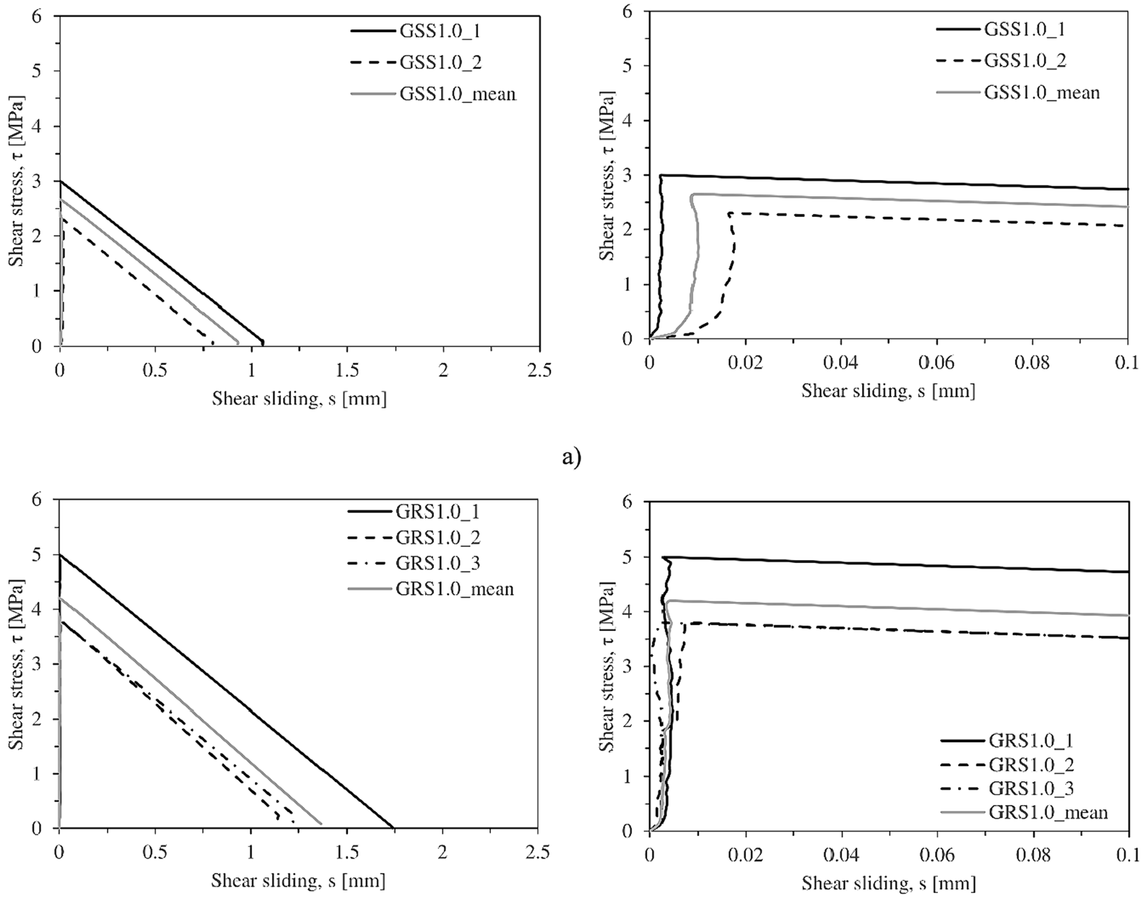

a)

b)

Fig. 4.5. Typical results of in-plane bond shear tests on FRS-granitic substrate with: a) smooth, b) rough surface of the substrate in contact with the FRS.

deformability of the masonry lining, as well on the maximum principal stresses in this tunnel structural component. The maximum downward movement (0.6 mm) occurred around the right-side arch, while the maximum compressive stress in masonry's spandrels is 2.14 MPa, which is much lower than the compressive strength of the granitic nature of the masonry arch (114 MPa).

In the second method, designated by "Strength reduction method", the material shear strength is successively reduced up to failure occurrence due to the attainment of a state of limit equilibrium. This method, which aims to determine the safety factor of the critical material parameters on a certain design scenario, was used to evaluate the critical zone around the tunnel. The vertical displacement field and the

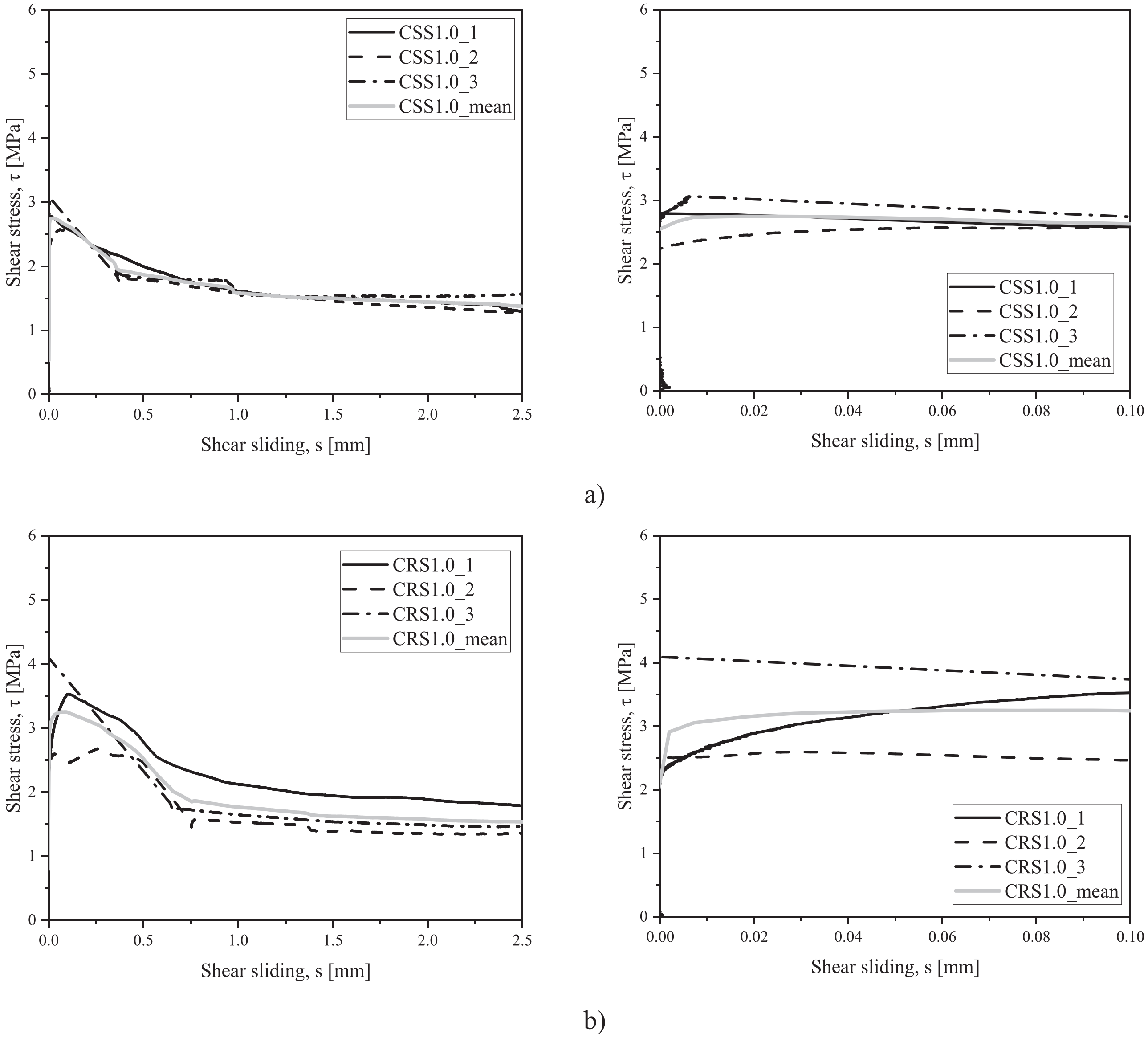

Fig. 4.6. Typical results of in-plane bond shear tests on FRS-clay substrate with: a) smooth, b) rough surface of the substrate in contact with the FRS.

maximum principal stress obtained using this method is represented in Fig. 5.7. In Fig. 5.7a, the maximum vertical displacement (2.7 mm) has occurred on the right side of the tunnel arch, which is in the same location provided by the stepwise method, although the displacement obtained in the second method is about 4 times higher than the first method. On the other hand, the maximum compressive stress in the spandrels of masonry's arch (Fig. 5.7b) is 0.5 MPa, which is similar to the value obtained in the stepwise method, whereas its magnitude is nearly a quarter of the stress in the first method. The different results obtained from these two methods can be attributed to the fact that in the stepwise method, the gradual reduction of properties is not applied to the masonry lining, while in the second method, the strength properties of the lining are also reduced along with the ground.

To determine the soil area surrounding the tunnel, whose soil-structure interaction is important to be considered to numerically assess the influence of an FRS strengthening solution on the stability of this tunnel (a topic covered in the next section), the displacements in a series of points along the axis represented in Fig. 5.8a were measured (vertical along z axis; horizontal along x axis). The top and bottom horizontal boundaries of the representative area were defined by the points where the vertical displacement was about 1/500 of the displacement registered in the crown and invert of the tunnel section (Points A and B). The lateral vertical boundaries of this area were defined by the point where the horizontal displacement was about 1/500 of the horizontal displacement in the face of the masonry arch (point C).

To simulate the most critical scenario for FRS structural strengthening, already proposed by Taheri et al. (Taheri et al., 2022), a zone of weak soil and a failing region soil was adopted, as represented in Fig. 5.8b, whose properties are presented in Table 5.2. In this scenario, and for these soil properties, the representative boundary conditions are those shown in Fig. 5.8c.

5.2. Meso modelling

Previously (Taheri et al., 2022), it was demonstrated that a thin FRS layer of 100 mm thickness, combining strain softening and strain hardening fibre reinforced concrete (SSFRC and SHFRC, respectively), can restore the loss of stiffness and load carrying capacity caused by the existence of a critical zone of soil with properties much lower than the remaining soil medium. That analysis was performed for the Mourilhe tunnel, by adopting the relevant conclusions of the simulations

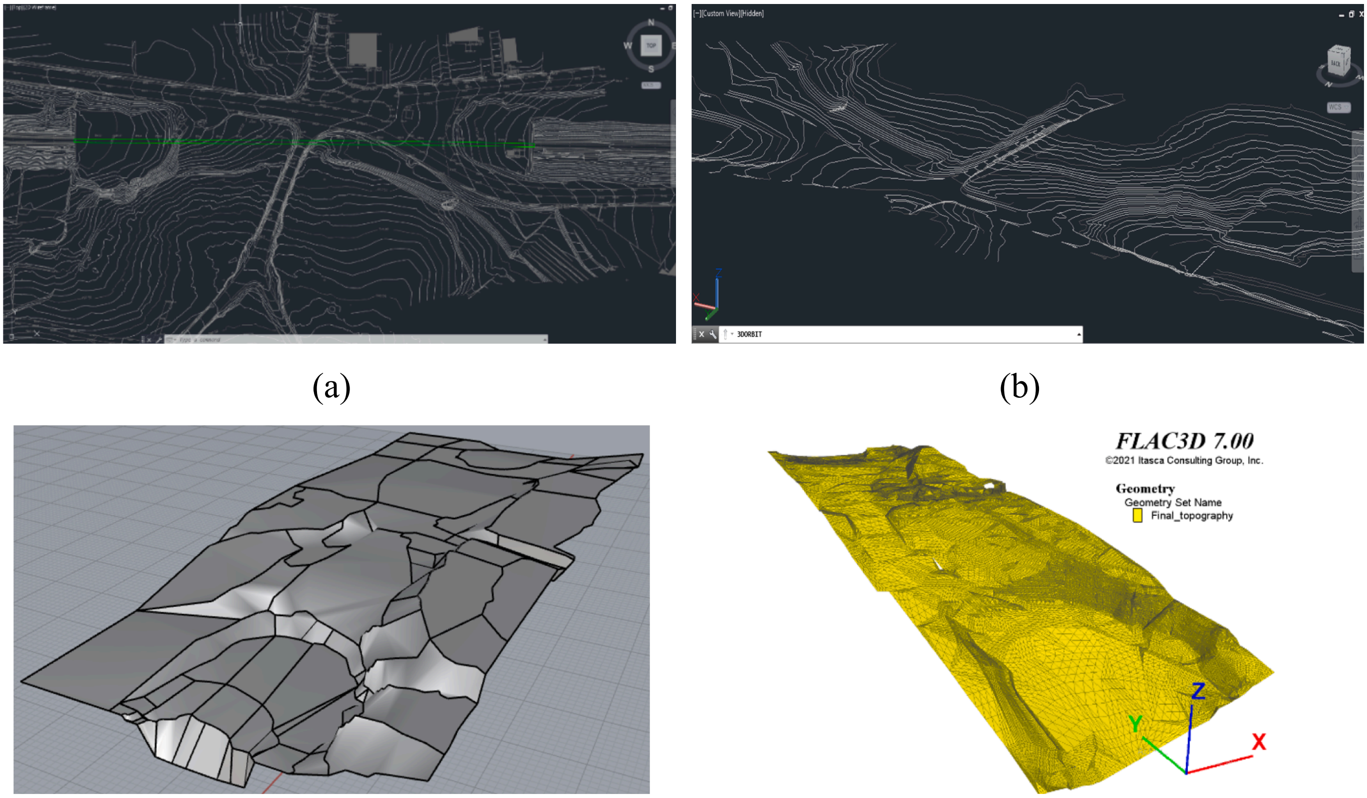

(a) (b)

(c) (d)

Fig. 5.1. A) topographical map with 2d contour lines in autocad, b) 3d contour lines in civil3d, c) 3d surfaces in rhinoceros, d) 3d mesh in flac^{3D}.

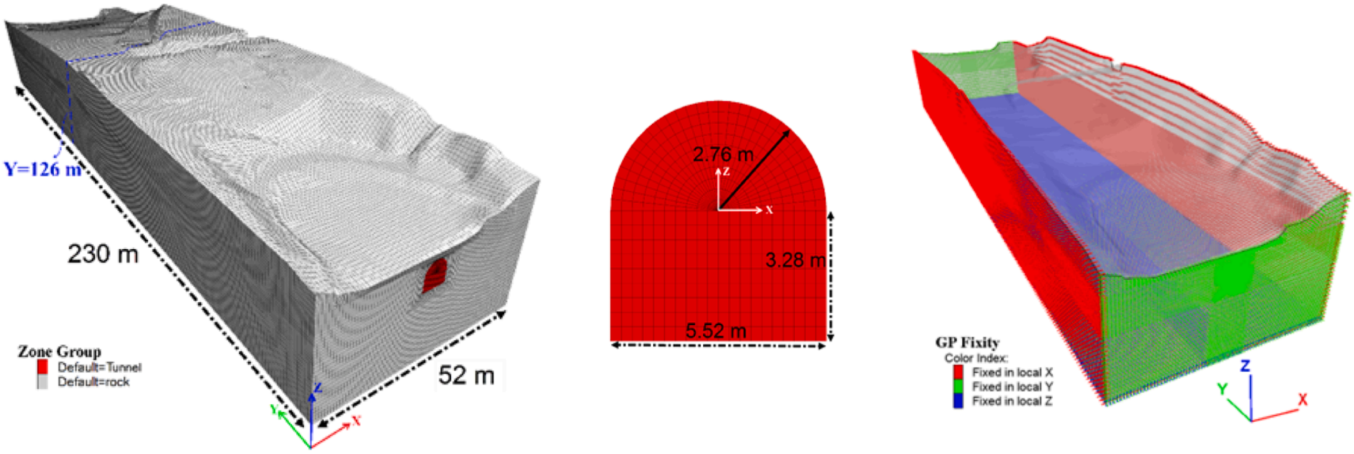

(a) (b) (c)

Fig. 5.2. A) three-dimensional geometry of mourilhe tunnel in flac^{3D}, b) Dimensions of the tunnel's cross section, c) Boundary conditions of the model.

Table 5.1
Estimated geotechnical parameters for simulating the Mourilhe tunnel with the Mohr-Coulomb model.

Parameter	E (GPa)	υ	Cohesion (MPa)	Friction angle (°)	Density (kg/m^3)	Compressive strength (MPa)
Weathered Granite	3.10	0.25	1.9	37.6	2700	69
Masonry Lining	40.27	0.25	2.6	42.0	2700	114

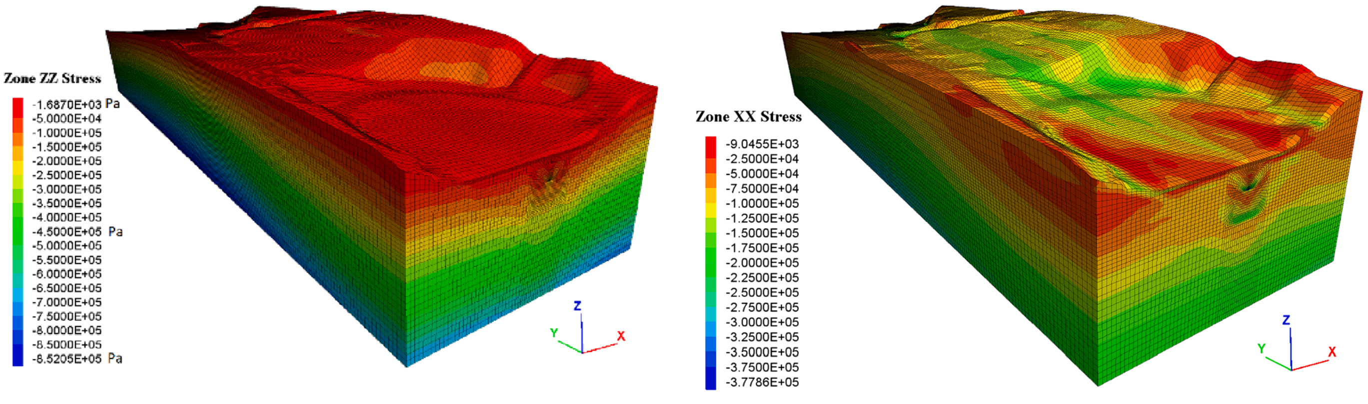

a) b)

Fig. 5.3. Initial conditions of the Mourilhe tunnel before excavation: a) initial vertical (in z direction) stress field (in Pa); b) initial horizontal (in x direction) stress field (in Pa) (Stress sign convention: positive value indicates tension; negative value indicates compression).

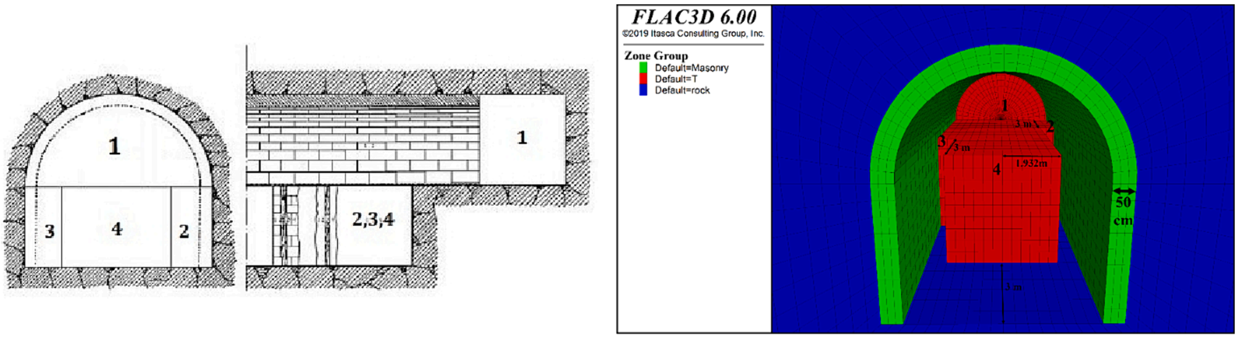

a) b)

Fig. 5.4. A) schematic representation of the belgian excavation method, b) simulation phases of belgian excavation method.

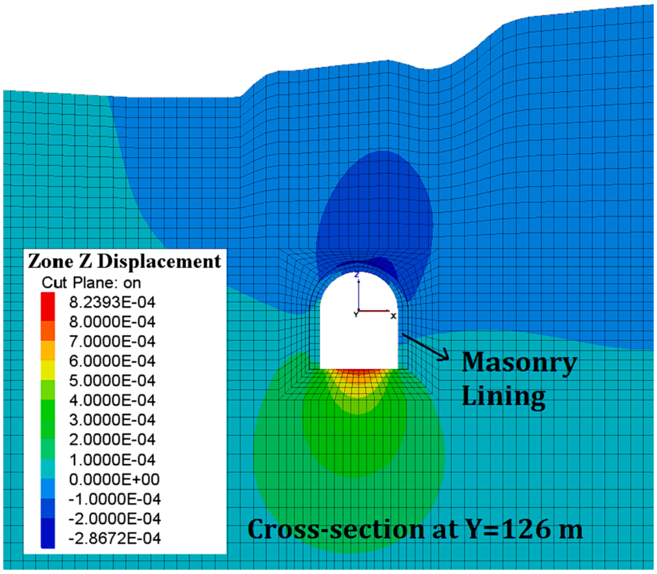

Fig. 5.5. Vertical displacement field in the transverse section of the model at Y = 126 m (in meters).

presented in the previous section.

By considering a representative tunnel's cross section and surrounding soil medium, determined according to the methodology described in the previous section, a meso modelling study was performed to assess the influence of simulating the contact FRS-masonry arch-soil and between the blocks forming the arch (Fig. 5.9). The influence of the loading conditions, the type of FRS (SSFRC and SHFRC) and their disposition in the layers forming the strengthening FRS shell, are also analysed regarding the tunnel's stiffness and load carrying capacity.

In a previous work (Taheri et al., 2022), it was demonstrated that, when the Mourilhe tunnel is submitted to the load type q_3 (Fig. 5.9), representing the dislocation of an unstable block of rock, the location of a weak soil in the zone represented in Fig. 5.9 is the one conducting to the highest loss of stiffness and load carrying capacity for this tunnel. In the present study, the following load cases were also considered: q_1, which represents a uniform distributed load in the total top boundary of the representative tunnel's section; q_2 that is also uniformly distributed in this boundary, but applied exclusively in the weak soil.

The numerical simulations were carried out with the FEMIX computer program (Barros, 2016), which has constitutive models capable of capturing the relevant nonlinear features of FRC, namely the fibre reinforcement resisting mechanisms after concrete crack initiation. The adopted finite element mesh is represented in Fig. 5.10, being formed by 8-noded plane stress elements with a 2 × 2 Gauss Legendre integration scheme for the FRS, masonry arch and soils. To model the contact between masonry blocks, blocks-soil, and FRS-blocks, line interface finite elements of six nodes with a Gauss–Lobatto integration scheme of 1 × 3 IP were adopted.

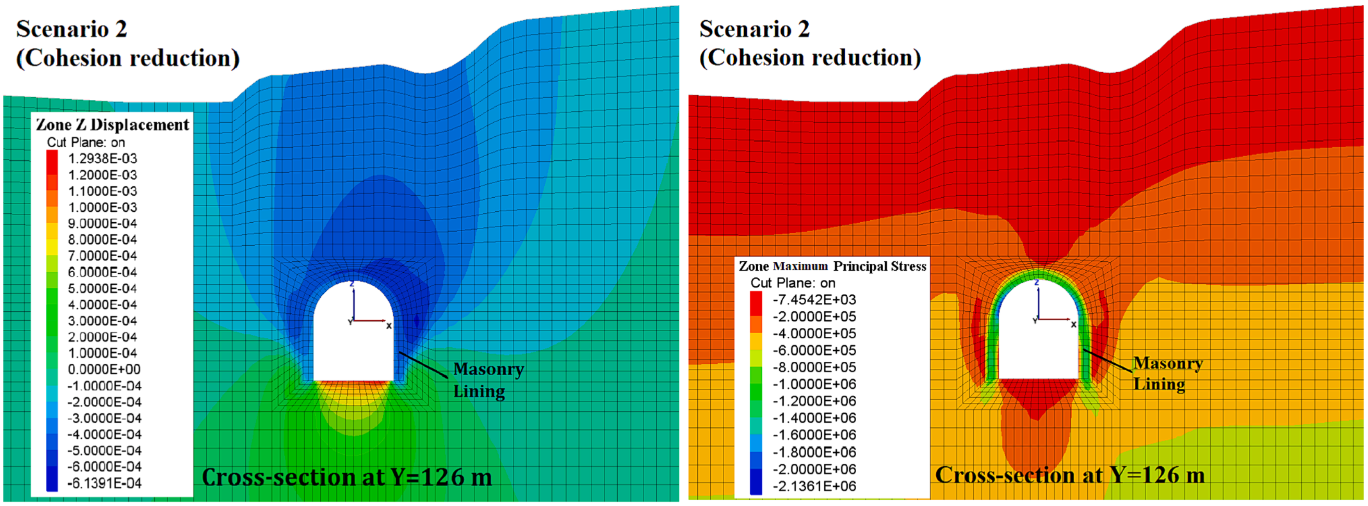

a) b)

Fig. 5.6. Results for scenario 2 at the tunnel's section Y = 126 m: a) Vertical displacement field in meters; b) maximum principal stresses in Pa. (Stress sign convention: positive value is tension; negative value is compression).

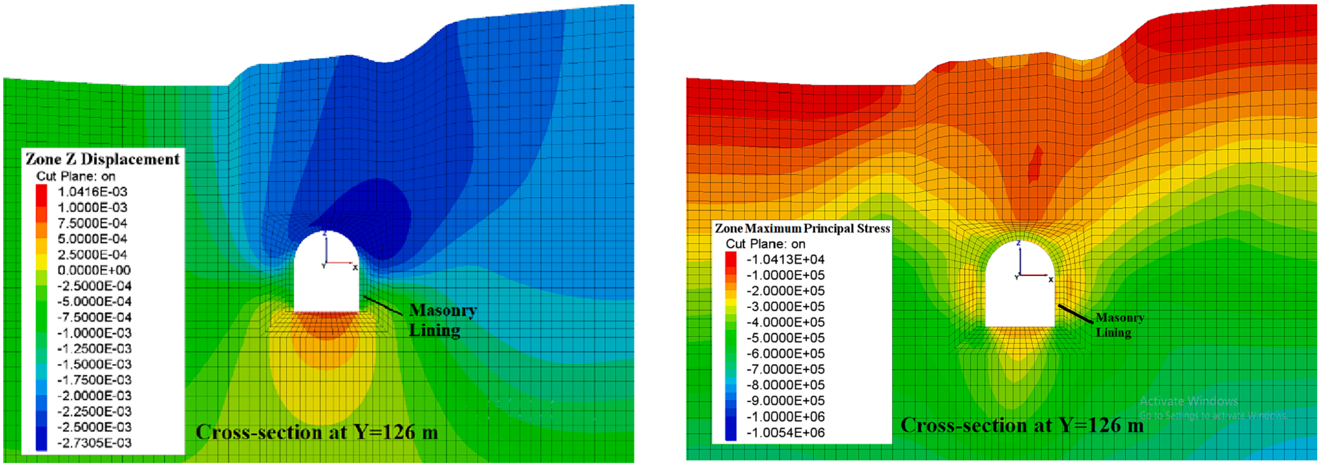

a) b)

Fig. 5.7. Results in the tunnel's section y = 126 m using the strength reduction method: a) Vertical displacement field (in meter); b) maximum principal stresses (in Pa) (Stress sign convention: positive value indicates tension; negative value indicates compression).

5.3. Constitutive models

The plastic/damage multidirectional fixed smeared crack model described elsewhere (Edalat Behbahani et al., 2015) was adopted for simulating the nonlinear behaviour of FRS in tension and compression, whose relevant diagrams are represented in Fig. 5.11 in order to illustrate the physical meaning of their defining parameters. Up to an effective stress (according to the William and Warnke failure surface (Willam and Warnke, 1974) of $\alpha_0 f_c$ (Fig. 5.11a) the FRS compressive behaviour is considered in linear-elastic regime, defined by the modulus of elasticity, E_c, and Poisson ratio, ν_c, of FRS.

According to the smeared crack model (SCM) of the adopted numerical approach, crack initiation and propagation is simulated by considering a cracked concrete as a continuous anisotropic medium. According to this approach, an increment of stress is obtained from an increment of strain via an elasto-plastic-cracked constitutive matrix, $\underline{D}^{epcrco}$ ($\Delta\underline{\sigma} = \underline{D}^{epcrco}\Delta\underline{\varepsilon}$), which integrates the information regarding the elasto-plastic behaviour of concrete in compression (yield surface, flow rule and evolution law for the hardening parameter), as well as the information corresponding to the fracture modes of the smeared cracks. The elasto-plastic component of this model is governed by the five-parameter Willam and Warnke failure criterion ($f = f(\underline{\sigma}; \overline{\sigma}_c)$), the flow rule $\Delta\underline{\varepsilon}^p = \Delta\lambda \partial f/\partial\underline{\sigma}$ ($\Delta\underline{\varepsilon}^p$ is the incremental plastic strain vector, $\Delta\lambda$ is the non-negative plastic multiplier), and hardening function $\overline{\sigma}_c - \tilde{\epsilon}_c$ represented in Fig. 5.11a.

Fig. 5.11b represents the diagram that simulates the concrete fracture mode I initiation and propagation, where is the tensile strength, is the mode I fracture energy, and define the shape of this diagram, and is the crack bandwidth. This last parameter correlates the crack width, w, with the normal crack strain, and is related to the size of the finite elements for avoiding the results be dependent on the refinement of the finite element mesh.

The sliding between the granitic blocks of the masonry arch, as well as between these elements and surrounding soil, is simulated from the following equation (Fig. 5.12a):

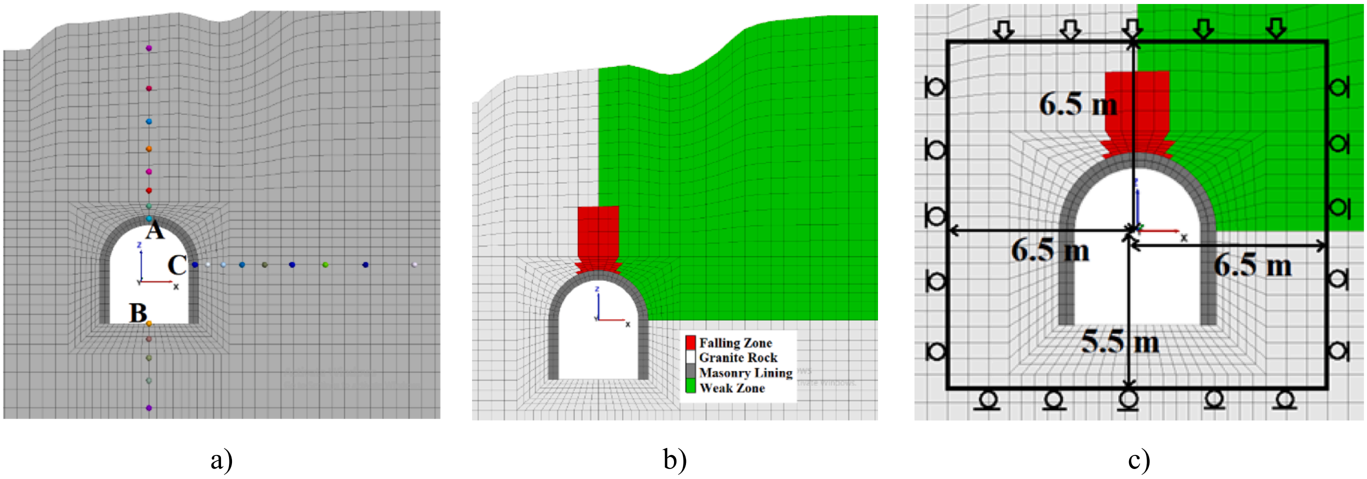

Fig. 5.8. A) adopting points for determining the representative tunnel's cross section for frs strengthening intervention, b) 2d view of the weak zone and the collapse region considered in the mourilhe tunnel model, c) dimensions of the representative tunnel's cross section for the frs strengthening scenario.

Table 5.2
Properties for the adopted materials.

Rock type	Elastic modulus (MPa)	Poisson ratio (-)	Cohesion (MPa)	Friction angle (°)	Density (kg/m^3)
Weathered Granite	3100	0.25	1.9	37.59	2700
Weak zone	31	0.25	0.95	37.59	2700
Falling zone	3100	0.25	0	0	2700
Masonry lining	40,270	0.25	2.6	42	2700

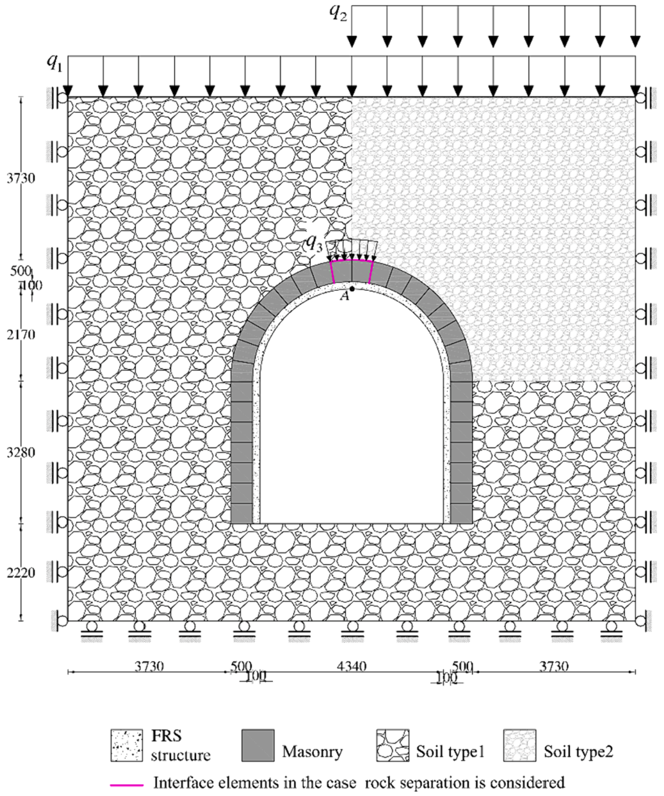

Fig. 5.9. Representative cross section of the Mourilhe tunnel, strengthening FRS structure, surrounding soil and loading and support conditions.

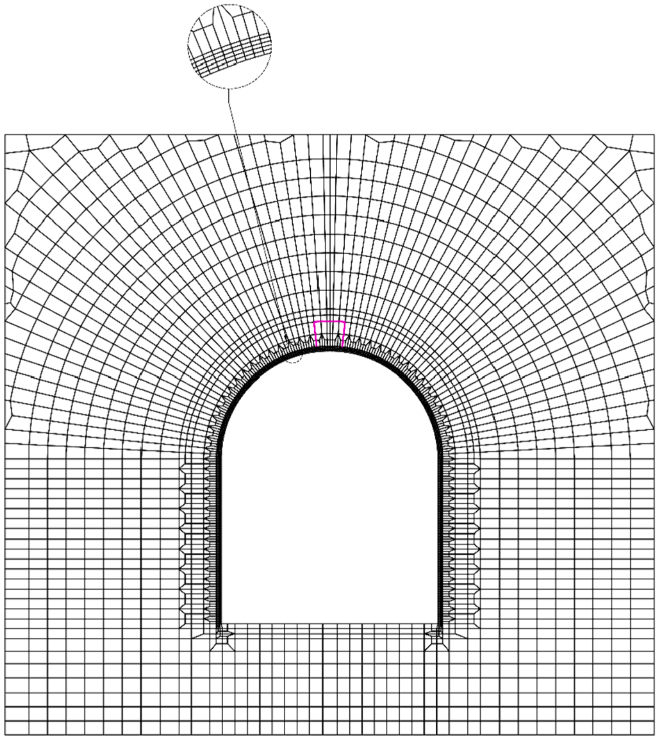

Fig. 5.10. Finite elements mesh considered in numerical simulations.

$$\tau = \begin{cases} \tau_0 (s/s_0) & s \leqslant s_0 \\ \tau_m (s/s_0)^{\beta_1} & s_0 < s \leqslant s_m \\ \tau_m (s/s_m)^{-\beta_2} & s > \varepsilon_m \end{cases} \tag{1}$$

where

$$\tau_m = c + \sigma_n . \tan\phi \tag{4}$$

with β_1 and β_2 being the parameters defining the shape of the $\tau - s$ branches between s_0 and s_m, and above s_m, respectively, while c and ϕ are the cohesion and friction angle of the interface, respectively. When using $\tau - s$, it is assumed the interface does not open, while when the movement of the interface is exclusively simulated by the $\sigma_n - w$, no sliding is considered and the stiffness before initiation of separation is defined by the k_n parameter (Table 5.5).

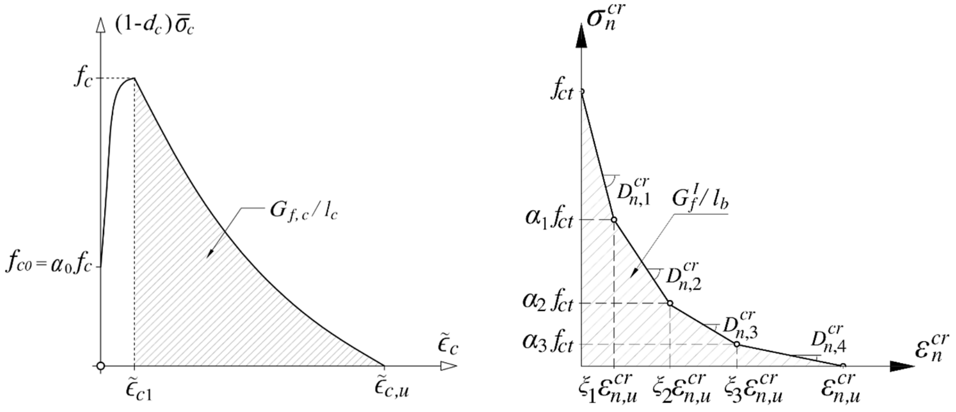

a) b)

Fig. 5.11. A) effective stress vs equivalent plastic strain in compression; b) crack normal tensile stress vs tensile strain ($G_{f,c}$: compressive fracture energy; G_f^I: mode I fracture energy; $l_c = l_b$ is the crush and crack bandwidth).

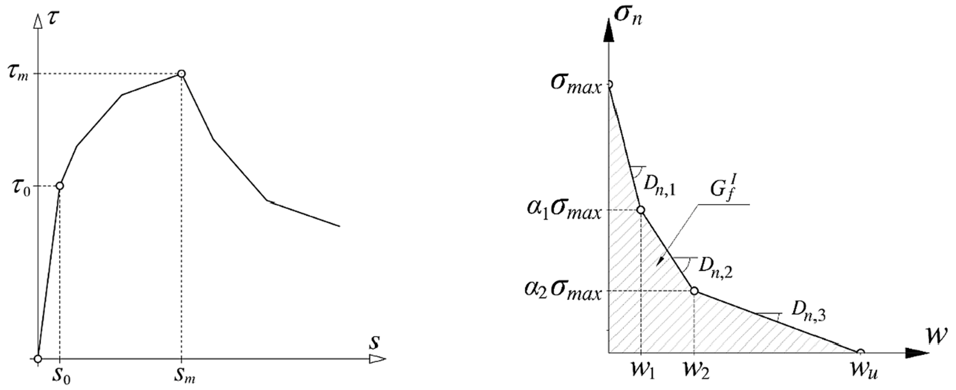

a) b)

Fig. 5.12. Constitutive laws adopted for the interface finite elements a) shear stress-sliding for modelling the contact between the blocks of the masonry arch and between them and soil b) Tensile stress vs opening displacement diagram for modelling the separation process between FRS shell and masonry arch.

Table 5.3
Constitutive laws of the used FRCs in numerical simulations.

Material designation	f_c (MPa)	f_{ct} (MPa)	E_c (GPa)	α_0 (-)	ε_{c1} (‰)	$G_{f,c}$ (N/mm)	α_1 α_2 α_3 (-)	ξ_1 ξ_2 ξ_3 (-)	G_f^I (N/mm)	V_f (%)	l_f/d_f (-)
SSFRC (Amin et al., 2015)	61.3	4.15	33.5	0.4	2.5	40	0.53 0.35 0.18	0.01 0.50 0.98	3.79	0.4	64
SHFRC (Redaelli and Muttoni, 2007)	190.0	8.90	60.0	0.4	3.5	60	1.09 0.65 0.22	0.04 0.14 0.25	23.50	2.4	125

V_f is the fibre volume percentage; l_f/d_f is the fibre aspect ration (fibre length/fibre diameter).

Table 5.4
Properties of the soils and masonry arch.

Material designation	E(GPa)	ν(-)	Density (kg/m^3)
Masonry (Granite rock)	40.27	0.25	2750
Normal soil	4.41	0.25	2700
Weak soil	0.05	0.25	2400

5.4. Material properties

For the FRS shell, the strengthening potential of possible arrangement with SSFRC and SHFRC was explored numerically. Their properties for defining the constitutive laws (Fig. 5.11) are indicated in Table 5.3. For the Poisson coefficient of both FRC, a value of 0.15 was assumed.

In these analyses, the soil and the granitic masonry arch were assumed in linear-elastic state, whose behaviour is defined by the

Table 5.5
Values of the parameters defining the $\tau - s$ constitutive model (Fig. 5.12a).

Bond designation	S_0 (mm)	S_m (mm)	C (N/mm^2)	∅ (°)	β_1 (-)	β_2 (-)	k_n (MPa/mm)
BS1	1.0	1.5	0.0	5.0	0. 5	0.7	1.0

parameters indicated in Table 5.4. To simulate a weak soil, a modulus of elasticity of about 1 % of the value adopted for the normal soil was assumed.

The $\tau - s$ simulating the sliding between the granitic blocks, and between these and the soil, in the critical region (Fig. 5.9 and Fig. 5.10), herein designated by BS1, is defined by the values of its parameters indicated in Table 5.5.

Several analyses were carried out to assess the influence of the different loading conditions (q_1, q_2 and q_3), and the consideration, or not, of the sliding of the masonry blocks in the critical region, in terms of loss of tunnel's load carrying capacity and stiffness. In all these analyses, the FRS shell was assumed to be formed by the SSFRC with the properties indicated in Table 5.3.

The most important analyses, herein designated by scenarios, are indicated in Table 5.6, and their corresponding load versus deflection is shown in Fig. 5.13. The load is the total vertical reactions, while the deflection is measured in point A (Fig. 5.9), considered positive in downward direction.

It is verified that the presence of the weak soil has a significant effect in terms of decreasing the stiffness, but the load carrying capacity is not affected, which is justified by the linear behaviour admitted for the weak soil. When comparing Scenario1 and Scenario3, it is verified the tremendous influence of the load case q_3. In this scenario, the q_1 was increased up to 1430 kN/m, and since then maintained, while q_3 was incrementally applied up to convergence difficulties in the numerical simulations forced to conclude the analysis. Comparing the responses of Scenario3 and Scenario4, it is verified the significant decrease of the stiffness when only q_1 is actuating, and a significant loss of load carrying capacity when q_3 was incrementally applied, which means that the possibility of the sliding between the granitic blocks of masonry in the considered critical region has a pronounced detrimental effect on the FRS strengthening efficiency, due to the higher cracking damage induced in the FRS shell (Fig. 5.14).

5.5. *Tunnels strengthening strategy for recovering its structural performance*

To assess the potential of using SSFRC and SHFRC in different layers of the FRS shell, applied according to the new robotic shotcrete technology, the strengthening region indicated in Fig. 5.15 was strengthened according to the three arrangements shown in Fig. 5.16. The SSFRC and SHFRC have the properties indicated in Table 5.3, and Scenario4 was adopted for the loading conditions, type of soils and contact modelling between the blocks of the masonry arch in the critical region.

The force–deflection obtained in these strengthening plans are compared to the ones determined in the Scenario3 and Scenario4. Fig. 5.17 shows that, by using only on layer of SHFRC in the outer faces of the FRS shell, the stiffness and load carrying capacity of this strengthening solution is identical to the structural efficiency of the other two solutions, but much more economic.. However, the stiffness registered in the Scenario3 was not possible to recover, since the difference in the modulus of elasticity of SSFRC and SHFRC is not enough to have an impact on the structural stiffness at this stage, and the thickness of the FRS shell was kept the same in all the analyses. To recover this loss of stiffness, the joints between the granitic masonry blocks should be filled by an adhesive that significantly increases the bond strength and the bond stiffness.

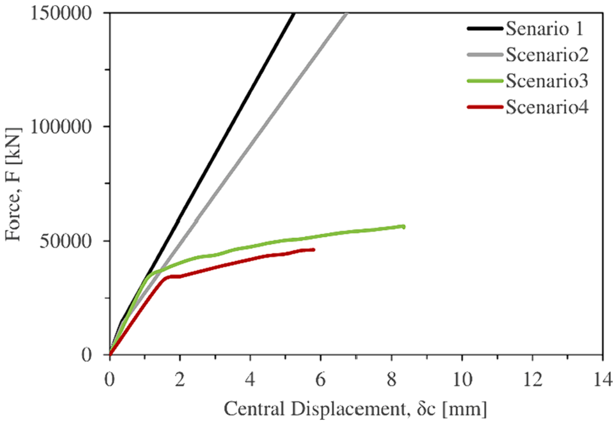

Fig. 5.13. Force-central displacement responses of Scenarios 1 to 4.

6. Control and automation for robot-assisted FRS

The shotcrete process yields a hazardous environment for the operator, requiring skilled manpower to achieve the thickness as specified by the structural stability project. Automating the projection will allow for a more accurate thickness control while enabling the variation of both the thickness and the FRS properties, since the amount of fibres in the FRS mixture can be adjusted in real time, according to the structural design, as described in the previous section. The sections below describe the developments to allow both the addition of fibres to ensure the aimed FRS properties, in real time, during the projection, and for the projection task to be automated. It should be noted that the concrete arriving to the shotcrete robot arm already includes a certain percentage of fibres, with an extra content of fibres being added in real time and during the projection, allowing to improve the properties of the FRS to accomplish the designed plan. This accomplishes the general requisites faced in structural strengthening with FRS, without dramatically increasing the technical demands for the innovative device that controls this operation.

6.1. *Development of fibre injection prototypes*

To have an effective shotcrete technology capable of applying, in real time, FRS with different properties, it is assumed that a premixed FRC is prepared according to a ready-mix concrete technology, with the properties for the areas of the RT with small structural demands in terms of strengthening intervention. This premixed FRC can already include

Table 5.6
Details of the adopted scenarios in tunnel simulation.

Scenarios	Soil type1	Soil type2	Masonry block relative displacement	Dead weight	q_1 (N/mm)	q_3*** (N/mm)
Scenario1	NS*	NS	–	Considered	Incremental	–
Scenario2	NS	WS**	–	Considered	Incremental	–
Scenario3	NS	NS	Considered	Considered	1430	Incremental
Scenario4	NS	WS	Considered	Considered	1430	Incremental

* Normal Soil; ** Weak Soil; *** q_2 was not considered since it was verified to be not so critical as q_3.

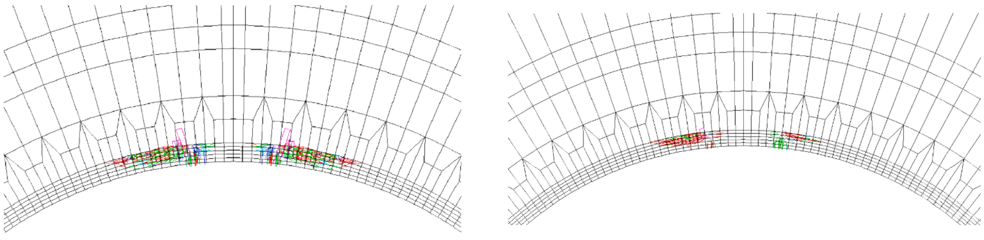

a) b)

Fig. 5.14. Crack pattern in the FRS shell at the maximum load level for the a) Senario3 and b) Senario4 (the red, green, dark blue, light blue, and purple represent a crack in opening, closing, closed, reopening, and fully-open status, respectively).

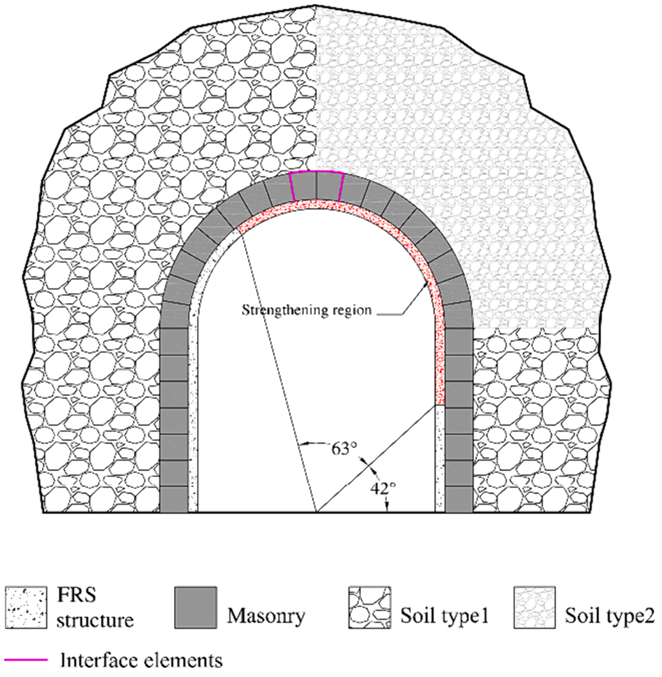

Fig. 5.15. Localization of the strengthening region.

more than one type of fibres, for instance, micro-polypropylene fibres and steel fibres, the first ones to avoid concrete explosive spalling in case of a fire in the tunnel, and the second ones to ensure the aimed post-cracking tensile capacity for the FRS. This FRC arrives to the new robot-shotcrete equipment, which incorporates a system for adding the amount and type of metallic fibres to ensure the FRS with the properties intended for the place being shotcrete. Such system should be located as near as possible of the projection head, ideally in the head itself, to minimize the delay between the fibre introduction moment and the projection instant. However, this possibility is difficult to achieve due to the inherent weight of both the fibres and the required mechanisms, bearing in mind the considerable amount to be introduced (between 15 and 30 kg of metallic fibres per m^3 of concrete). The alternative is to build this system as near as possible to the robot's base, minimizing the mentioned delay and sharing the load bearing structure of the robotic arm. Due to the reasons to be explained later, in the present phase of this project, only metallic fibres will be added to the premixed FRC.

6.1.1. *Mechanism to add the extra content of fibres to the FRS*

To add the extra content of fibres to the pre-mixed FRC that comes to the robotic shotcrete arm, an electro-mechanical mechanism has been conceived, built, and tested, which, due to its inherent complexities, has been subject to an iterative process with successive implementations and improvements. The appropriate content of fibres to be added depends on the instantaneous FRS flow in the pipe. Due to the pulsating flow generated by the concrete pumping system being used, this becomes rather difficult to achieve. On the other hand, the fibres are to be introduced at a point where the concrete pressure may be more than 20 bar, which demands a robust mechanism from the mechanical point of view. The first trial on the development of this mechanism was based on sensing the instant flow and controlling a motorised fibre introduction system. The simulations during the design process have, however, showed that this approach would not be able to comply with the expected demanding operating conditions. The second trial was based on a self-propelled rotor with variable volume chambers, able to guarantee the fibre-to-concrete ratio independently of the instantaneous flow. A

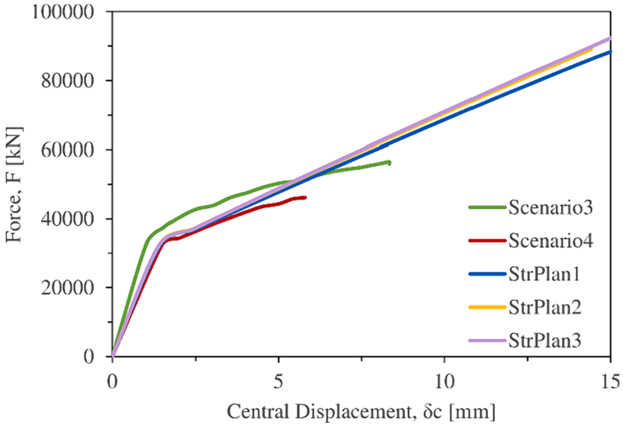

Fig. 5.17. Comparison of the force-central displacement responses of Scenario3, Scenario4 and of the three strengthening plans.

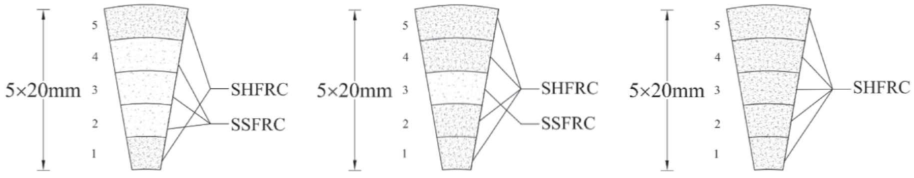

a) b) c)

Fig. 5.16. Cross-sections considered in the strengthening plans of a) StrPlan1, b) StrPlan2, and c) StrPlan3.

first prototype of this mechanism was built, and the tests carried out demonstrated the need for some improvements, which is an ongoing task.

In what concerns the first design, it is based on a cam mechanism guiding fibre injection into the concrete through cylinders. The reciprocating motion of the pistons depends on the rotation of the rotor and pins, with bearings mounted on the endpoints of the piston structure. The piston motion is guided by a cam system, which was constructed by combining two cylindrical structures with specially designed slots, or guides, as shown in Fig. 6.1.

This design showed two main problems: 1) The mechanical design was complex and with some potential fragile spots; 2) The ability of fibres insertion was not compatible with the short pulses (2–3 s) of the pumped concrete flow. Moreover, the possible solutions for flow measurement were either not appropriate or too expensive to be used in the project's scope.

The second concept is based on the principle of a rotary set of variable volume chambers propelled by the flowing concrete (see Fig. 6.2). The pressure loss of such mechanism, which could be an obstacle in principle, is not relevant, since the power of the pumping system is enough to rise the concrete over more than 17 m, and the maximum projection height for the operation within the project is well under 5 m. In this design, the concrete flow pushes a blade that encloses a fixed volume of concrete into which the content of fibres, required by the structural design project, is introduced. The rotor is divided into four different zones by collapsible blades that allow the separation between the high-pressure zone, where the concrete flows, and the atmospheric pressure area, where the fibres are introduced. This way, the fibre-to-concrete ratio is maintained, independently of the actual instantaneous flow rate, since the rotation speed of the rotor, and, consequently, the opening and closing of the fibre introduction vent, will directly follow flow variations. The solution, the principle of which is depicted in Fig. 6.2, becomes simpler, since no sensing, motoring, and controlling devices are needed at this stage. Therefore, the control of the fibre content to be added is concentrated solely within the dosing mechanism where the high-pressure concrete is not present.

6.1.2. *Fibre separation system*

With the proposed fibre introduction mechanism, the rate of fibres to be added into the self-propelled system must be controlled prior to insertion. The abovementioned concept implies that the appropriate amount of fibres (in accordance with the structural design project), is measured and is ready to be introduced whenever the rotor movement opens the input window. This timing depends on the actual rotation speed, which is set by the instantaneous flow rate of the pumped concrete. A second issue to overcome is avoiding the tendency of fibres to entanglement, which can block the flow of the FRS into the mixing device. This problem is common to all type of fibres, but more critical with the metallic ones due to their higher stiffness, compared to the polymer ones. As such, the fibres dosing mechanism should have the following four different functions: 1) prevent fibres entanglement; 2) ensure a controlled variable flow of fibres; 3) control the correct weight of each fibre batch to be dropped into the mechanism's intake port; 4) synchronize the fibres dropping process with the variable rotation speed of the rotor. The first function is ensured by introducing two moving conveyor belts (see Fig. 6.3) within the feeding section of the hopper. By moving the belts in opposite directions, the fibre mass is in constant motion, effectively preventing entanglement. Gravity will do the rest by allowing the fibres freed by this motion to fall through the gap between the belts. The control of fibres addition is achieved by the uplifting belt speed, which results in more fibres being separated from the entangled mass; 2) the gap between the belts can be increased, allowing higher content of fibres to feed the hopper. The control of the mass of fibres in each batch is achieved by using a dosing cylinder mounted on a load cell. Finally, the target mass of fibres is dropped into the mixing box by rotating the dosing cylinder by a quarter of a turn.

To evaluate the amount of metallic fibres in a certain volume of concrete, a metal detector was designed. This detector is formed by a two-coil transformer capable of measuring the mass of the metallic fibres going through the sensor. The primary coil is fed with a sinusoidal voltage creating a magnetic flux that induces a current on the secondary coil. The effective voltage measured at the output on this secondary coil depends on the magnetic coupling between both coils, which is influenced by the core material. The core is a variable mix of air and metallic fibres, and the coupling increases with the metal-to-air mass ratio.

Torrents et al. (Torrents et al., 2012) performed a series of prototype tests using inductive methods, to evaluate fibres' orientation in fresh concrete cubic specimens and using a low-impedance analyser. Despite explaining the process using a two-coil transformer, they analysed the change in the self-inductance of a single coil to perceive the number of existing fibres. In another approach, Nunes et al. (Nunes et al., 2016) proposed an inductor with a U-shaped ferrite core with a single coil winding the ferrite's two legs, to determine the content and orientation of steel fibres in concrete on thin slab samples. The idea was to assess the content and the orientation of the fibres into a certain volume of concrete. The authors formulated a circuit simplification of the set coil and

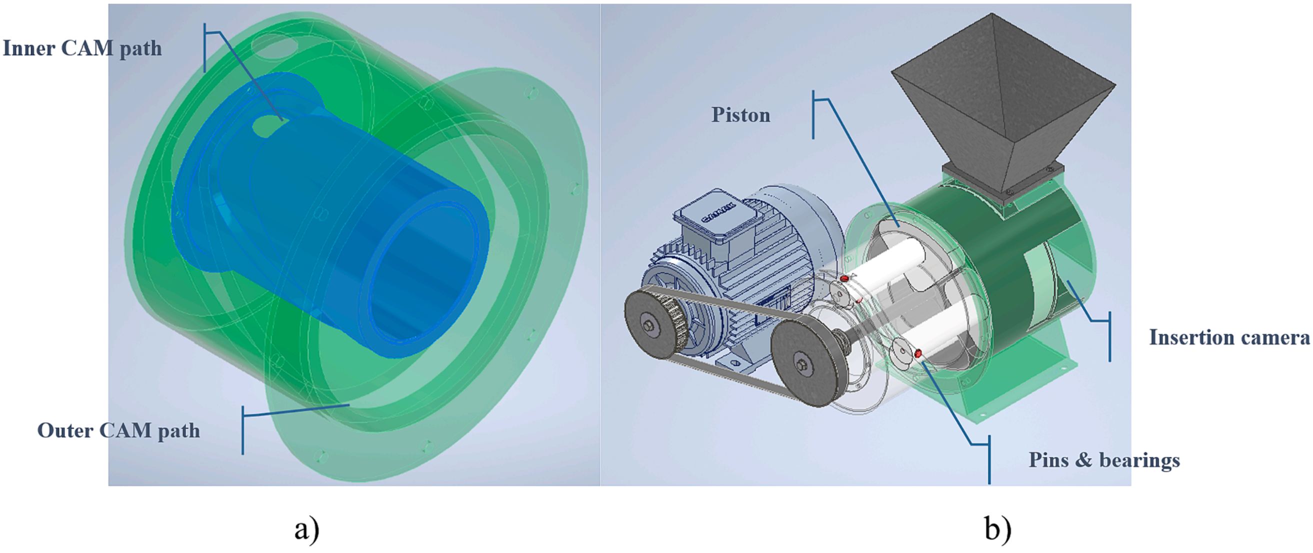

Fig. 6.1. First design: a) cam paths, b) full view.

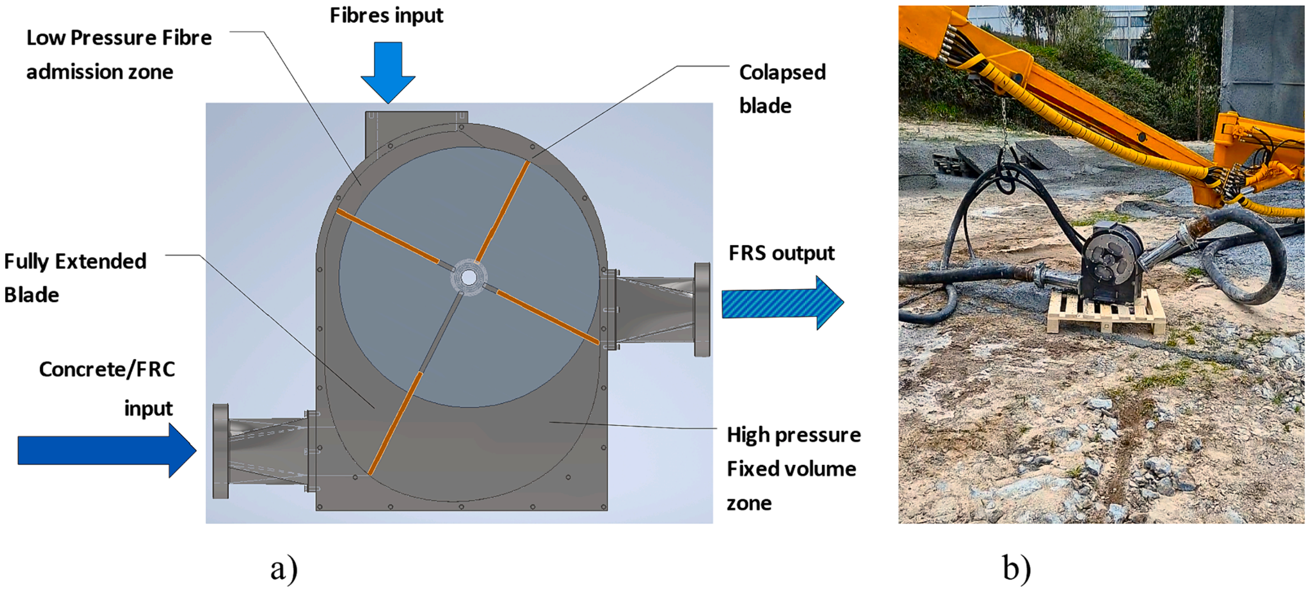

Fig. 6.2. Self-propelled system: a) concept, b) first built prototype being tested.

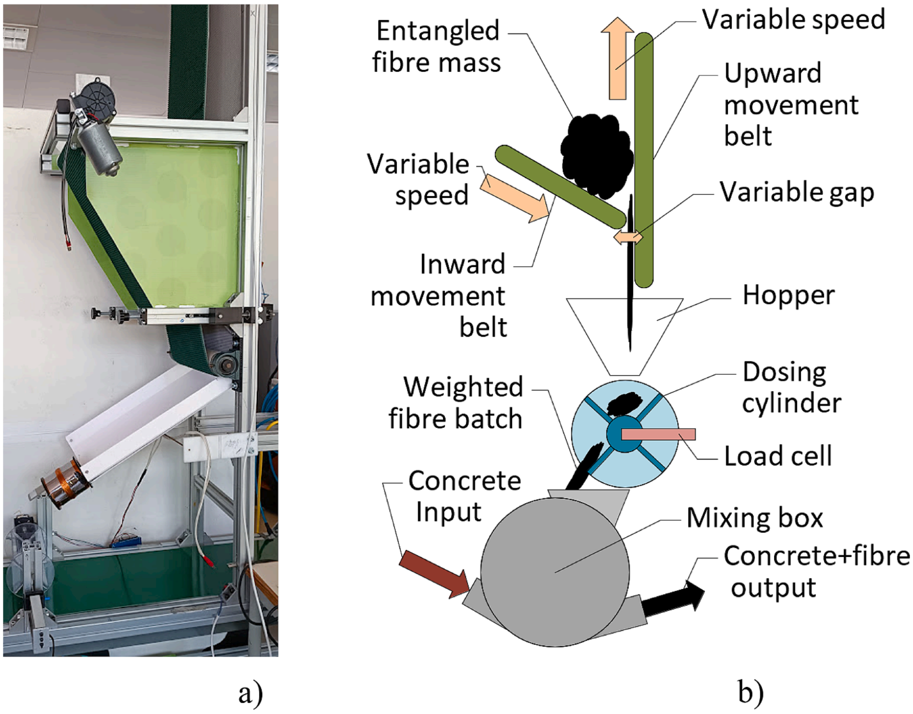

Fig. 6.3. Fibre entanglement avoidance mechanism Right: Operating principle; Left Physical prototype.

concrete slab, to measure the coil's inductance within both axes of the slab. They concluded that the orientation of the fibres could interfere with the measurements of the fibre content. The prototype proposed here uses a primary coil with 600 turns with a 15.63 mH inductance, and a secondary coil with 50 turns and 6.23 mH inductance. The test voltage applied to the primary terminals was 10 V at 100 Hz. Varying the input signal frequency demonstrated that the output on the secondary coil also changed, due to the resonant frequency, when the two coils are excited with a specific coupling frequency that amplifies the transformation on the secondary to enhance the output signal. This careful choice of input frequency allows a higher sensitivity in the device. The overall block diagram proposed for the instrument is shown in Fig. 6.4.

Its operation can be described as follows: the primary loop is excited using an AC voltage of known amplitude and frequency; then, a voltage measurement is performed on the secondary coil; the passage of the metallic fibres through the interior of the detector modifies the characteristics of the electromagnetic field and the measured voltage according to the content of fibres; this raw signal needs to be conditioned, which was ensured by a filtering and amplification process, before being acquired and processed by an appropriate device (microcontroller, PLC, or computer). From the specified device, it is possible to control the fibre input, as depicted in Fig. 6.4, closing the control loop.

6.2. *Tunnel surface scan and post-projection analysis*

Monitoring the tunnel structure before and after the projection is

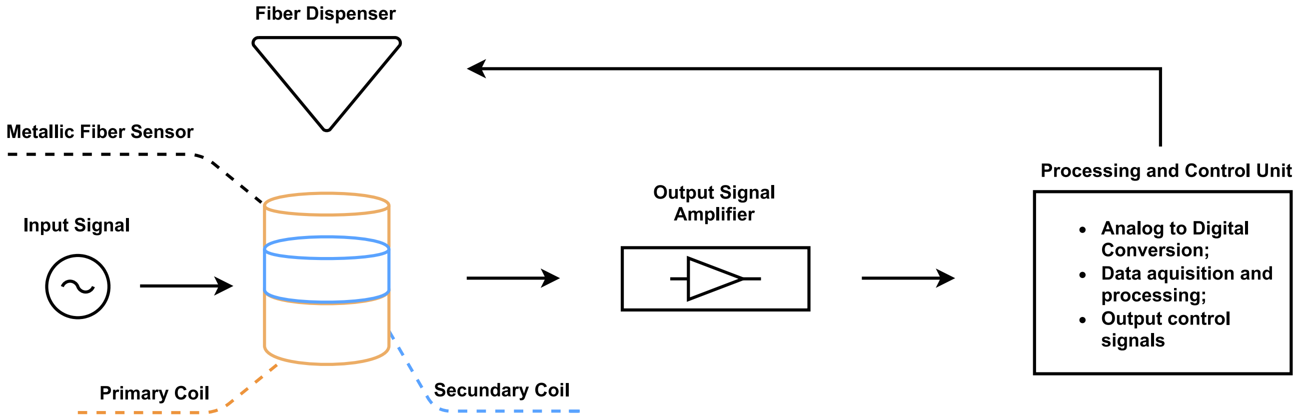

Fig. 6.4. Proposed overall block diagram for the detector of content of steel fibres in a certain concrete volume.

required to guarantee a uniform layer thickness of the projected FRS, to detect imperfections and apply corrections if needed.

Monitoring the tunnel structure is achieved by performing laser scanning using Light Detection And Ranging (LiDAR) devices. These devices output multiple points that represent a distance to the sensor, thus allowing to generate a point cloud with a level of precision dictated by the equipment itself, and the materials being scanned. For a moving platform, the automatic alignment of the received point clouds is required to generate an accurate digitalization of the structure. Otherwise, all the received data, independently from sensor location, would be registered to the same reference frame, resulting in an inaccurate representation of the structure. To perform the alignment of the received point clouds, the Simultaneous Location And Mapping (SLAM) algorithm was implemented. This algorithm allows to perform mapping while keeping track of the platform motion, often making use of registration algorithms (Zhou et al., 2021; Sensors, 2022) to register the received point data and to create a global point cloud that accurately represents the tunnel surface.

Point cloud registration is also required to align the generated point cloud of each scan, as these can have a distinct reference frame. One popular algorithm for point cloud registration is the Iterative Closest Point (ICP) (Besl and McKay, 1992), which is a method to register two-point clouds by iteratively minimizing the distance between their corresponding points. A concise and straightforward illustration of the entire procedure is shown in Fig. 6.5.

Registering large scale point clouds demands increased computing power. To enhance registration efficiency, one effective approach is to use a specialized data structure such as octrees (Eggert and Dalyot, 2012). Octrees work by recursively dividing the 3D space into increasingly smaller cubic cells, where each cell is subdivided into eight neighbouring cells, forming a hierarchical structure that are mutually connected. This data structure (illustrated on Fig. 6.6) is designed to efficiently represent a three-dimensional space, where each node, at any given depth level, can be divided into eight child nodes through a regular 2 × 2 × 2s ubdivision, or it may have no child nodes. Inherent to this structure is a key relation between the octree depth level and its spatial resolution. Specifically, with each successive subdivision level towards a finer refinement, the spatial resolution in each of the three dimensions (i.e., length, width, and height) is effectively doubled. This is due to the fact that, at each depth level, the spatial domain is subdivided into eight smaller, equally sized volumes. Therefore, the refinement level in an octree dictates its spatial resolution, with higher depth levels corresponding to higher spatial resolution. This feature allows the octree to adaptively represent spatial data with varying levels of detail, providing a finer resolution where it is needed, while conserving computational resources elsewhere.

The tunnel presented in Fig. 6.6 is colour coded by the geometric distance between two octrees, each constructed from laser data acquired sequentially, one prior and other after the concrete projection.

The software required for the described functionalities runs under the Linux operating system, on top of the Robot Operative System (ROS) (Quigley, et al., 2009). In ROS, software and sensor drivers can send and

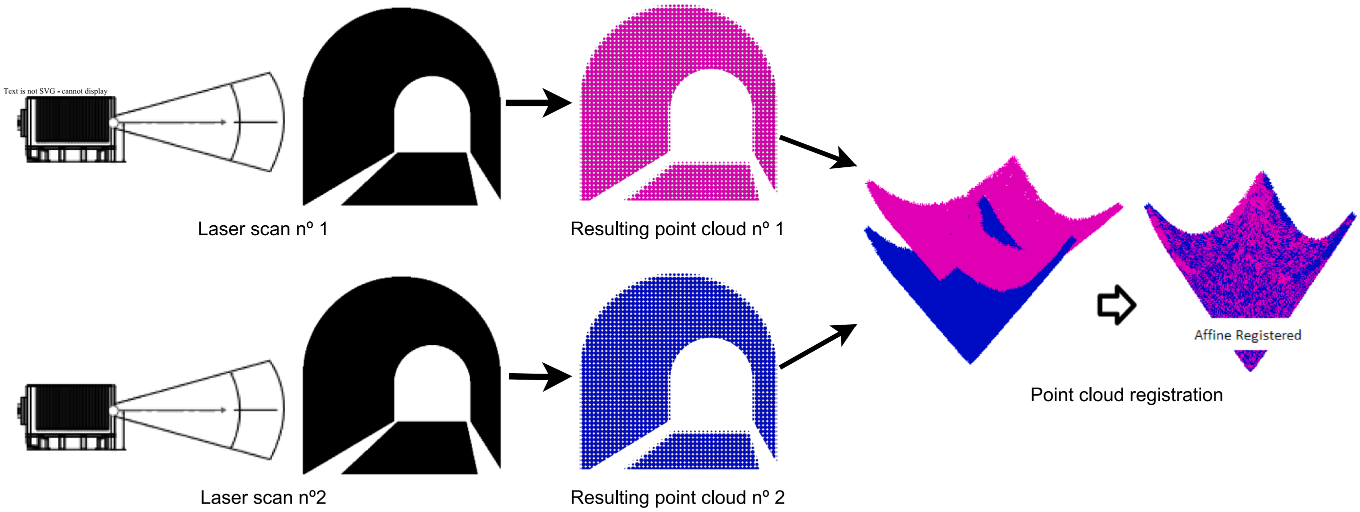

Fig. 6.5. Illustration of the tunnel laser scanning and registration process.

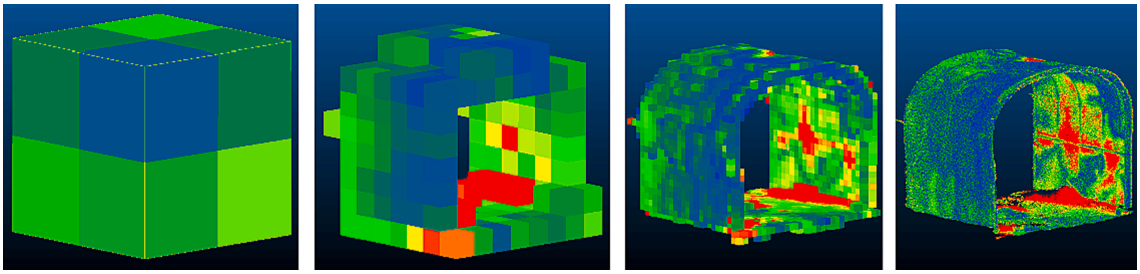

Fig. 6.6. Illustration of octree depth levels: from coarse to fine refinement.

receive information using messages These "messages" being published or subscribed in a stream of data, designated as *"topics",* henceforth will be designated as *"data stream"*. The developed software, that automates the process of capturing and comparing point clouds, runs as a ROS package. The point cloud messages published by the LiDAR's ROS driver are subscribed by the running SLAM algorithm. This SLAM algorithm then estimates the sensor motion by analysing the current and past LiDAR messages, a process known as LiDAR odometry. After performing LiDAR odometry, point cloud messages are registered to the global map. The registered point cloud messages are published by the SLAM algorithm to a specific *"data stream"*. An implementation of the Point Cloud Library (PCL) ROS implementation subscribes the *"data stream"*, saving a point cloud file for each received message. When the tunnel laser scanning is completed, the point cloud files are merged into a single full tunnel scan file. To obtain a global point cloud for the time before and after the FRS projection, the previous process is performed twice.

After converting the point clouds of the instances, from before and after the FRS projection to octree representation, registering between the two point clouds is performed using the ICP algorithm.

To compute the distance (difference) between the two octrees, the initial octrees is selected as the reference octree, and an octree-to-octree distance calculation is performed. An octree-to-octree distance consists of computing the distance of a given octree leaf relative to the closest octree leaf on the reference octree. As a result, a new field is added to each leaf of the compared octree, which contains the distance (in meters) of the octree leaf relative to the closest octree leaf on the reference octree.

One of the FRS projection experiments carried out on the prototype tunnel is shown in Fig. 6.7a and Fig. 6.7b, for the tunnel inner surface, before and after projection, respectively (the experiments were conducted using a Livox Horizon LiDAR, which features a distance random error of less than 2 cm at 80 % surface reflectivity). Each figure shows a photo of a tunnel prototype (purposely built for testing within this project by the partners EPOS and Leirimetal), as well as the generated

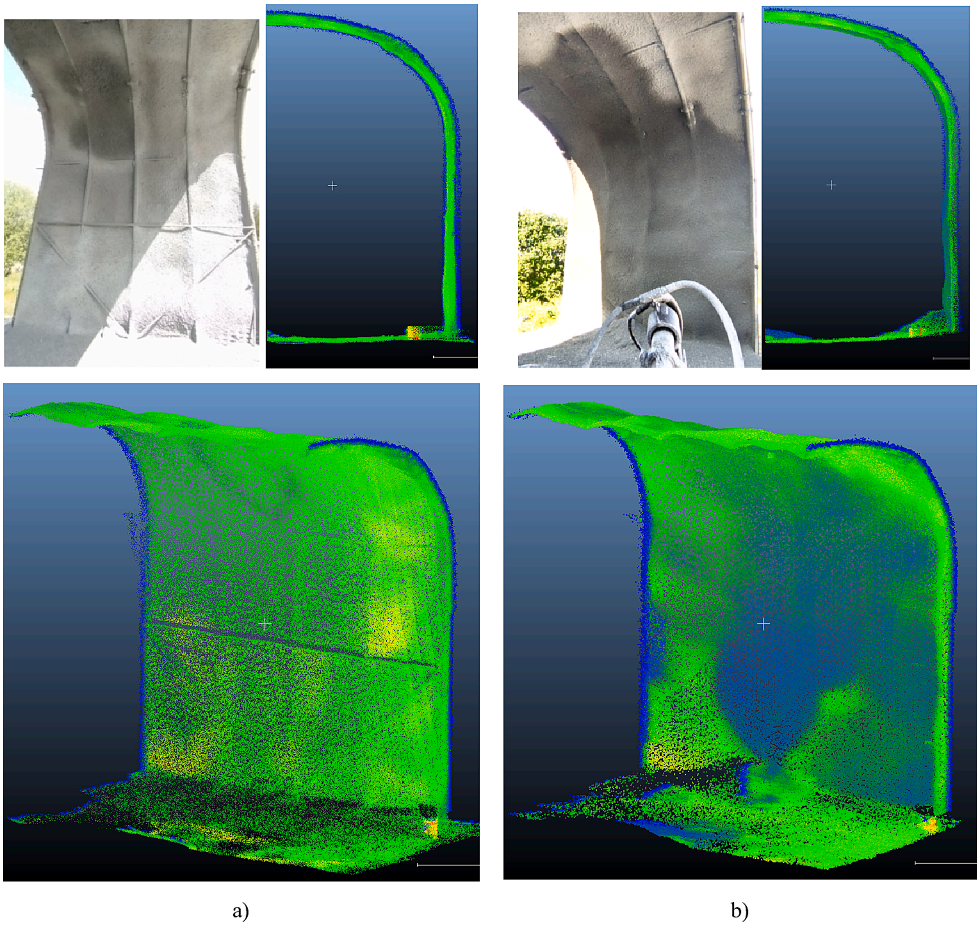

a)

b)

Fig. 6.7. Prototype tunnel experiment before a) and after b) projection

octree from two different perspectives. The colour of these point clouds represents the intensity of the received light for each respective point, with a darker colour indicating lower intensity. The displayed colours follow a linear scale of blue, green, yellow, and red, from minimum to maximum intensity, respectively. Fig. 6.7a and Fig. 6.7b colour scales have intensity values from 0 to 98, and 0 to 85, respectively. The highest possible value for the intensity parameter is 255, which is only reached with a very high reflective surface.

By scanning the surface with the LiDAR, a model of the tunnel was constructed for the instances before and after the FRS projection. The differences that occurred in the tunnel surface model were computed from the point cloud derived from each scan. The resulting difference can be visualized by attributing a colour to each octree leaf, which represents leaf to leaf distance, using as a reference the initial octree. As an example, Fig. 6.8 shows the difference for the obtained point clouds from the experiments shown in Fig. 6.7.

During the mentioned experiment, FRS was projected to one half of the tunnel only, hence all the figures are showing only that half. In Fig. 6.8a, the difference between the surfaces is shown, with a linear colour grade that ranges from the minimum measured distance (0 cm) to the maximum measured distance (31.44 cm). In Fig. 6.8b, the linear colour grade was applied to the points with a distance ranging from 1 to 4 cm, to better enhance the differences in this interval. Seven iterations of the experiment were performed, where FRS was projected to a fixed point of the tunnel wall, as shown in Fig. 6.9a, with the corresponding scanned point cloud being shown in Fig. 6.9b and Fig. 6.9c. The depth of the projected blob was measured by inserting an analogue depth gauge, with sub centimetric precision, into the recently projected FRS. The blob was then removed from the structure and the surface rescanned prior to the next projection.

From the scanned point cloud, the area of the projected FRS was extracted, as shown in Fig. 6.9c. After computing the difference between point clouds resulting from each extracted area, (shown in Fig. 6.10) for each of the experiment seven iterations, the implemented algorithm extracts each point with its corresponding distance parameter.

The extracted points are then sorted from lower to higher distance, and a histogram is created. By recursively identifying the statistical mode of points closer to the maximum measured distance, the projected FRS blob maximum depth is estimated. The fourth FRS projected blob detached from the wall due to its own weight, hence its scan and characteristics are not being shown. From the results shown in Table 6.1, one can observe that the differences between the LiDAR blob depth estimation and the analogue depth gauge measurements always fall within the LiDAR's 2 cm precision.

A surface with high reflectivity percentage will provide more accurate results. For reference, the reflectivity of most points on the point clouds at Fig. 6.7a and Fig. 6.7b range between 7.4 % and 19.2 %, and between 4.0 % and 16.7 %, respectively. The currently in-use LiDAR sensors will be replaced in the future with more recent LiDAR sensors, such as the Ouster OS1 Rev 7, which features a precision near ± 0.5 cm for 10 % surface reflectivity. This LiDAR will enable a higher resolution in inter layer thickness assessment and, consequently, more flexibility for the project contractor when defining concrete layers thickness.

6.3. *Trajectory generation and execution*

The shotcrete machine must automatically generate and follow a path for the process to be fully automated. This subsection describes how the path generation and execution works, which follows the pipeline summarized in Fig. 6.11. The details of each step are provided in five subparts, as follows: 1) creation of the cartesian path; 2) path adaptation to avoid collisions; 3) search in joint space to obtain a path feasible exclusively by linear motions; 4) simulations to estimate the result of the projected shotcrete layers; and, 5) trajectory execution using communication with the controller through TCP/IP.

6.3.1. *Generation of the cartesian path*

Assuming the TCP (Tool Centre point) is located on the axis that passes though the nozzle, with a displacement from the nozzle tip (away from the robot) equal to the desired nozzle-to-wall projection distance, the cartesian path for the TCP to follow must be composed of targets whose position lie on the tunnel surface. The cartesian path is created based on a mesh that represents the tunnel inner surface, such as the ones described in Section 6.1. The algorithm allows generating four different path types, namely straight, straight with ellipses, square-wave, and square-wave with ellipses, as shown in Fig. 6.12. The path to be selected, and its parameters, should be the one that ensures the thickness of each projected layer along the tunnel surface, according to the structural stability project, something that will be further discussed later. Each path has a different set of parameters that need to be

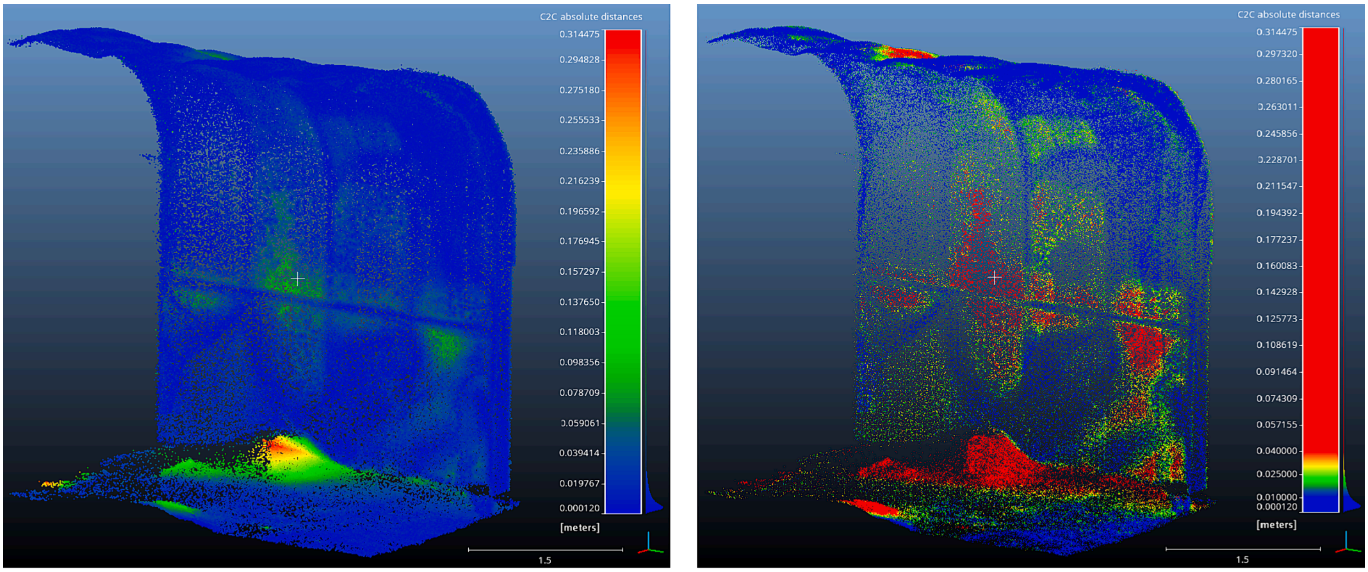

a) b)

Fig. 6.8. Difference between scans in meters: a) linear colour grade range [blue, red] = [0, 31.44]cm; b) linear colour grade range [blue, red]=[1, 4] cm.

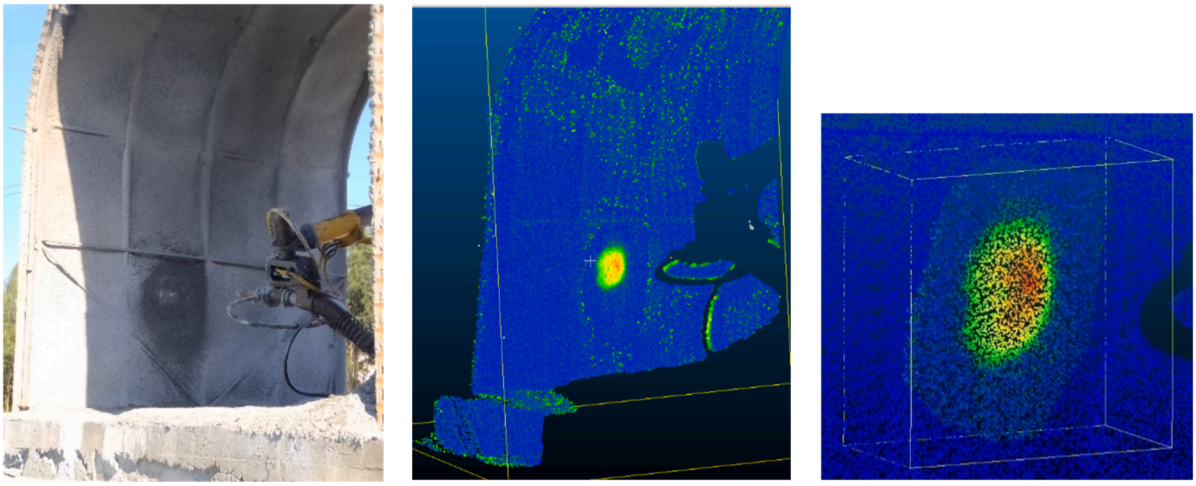
a) b) c)

Fig. 6.9. Tunnel surface after single point projection.

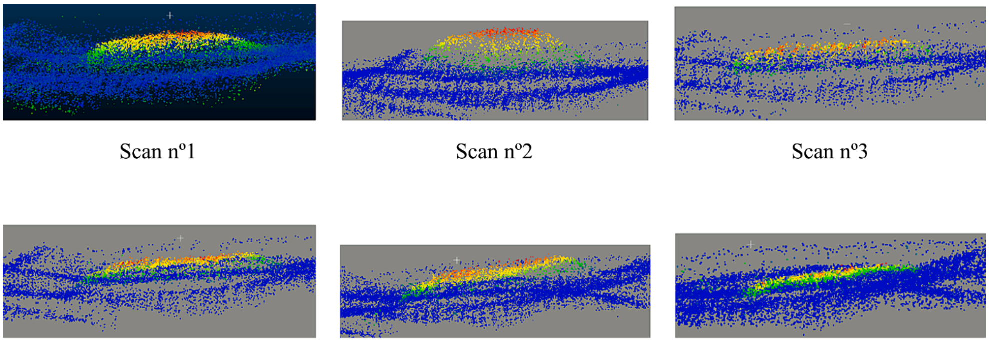
Scan nº1 Scan nº2 Scan nº3

Scan nº5 Scan nº6 Scan nº7

Fig. 6.10. Lateral view of projected FRS.

Table 6.1
Results from the FRS concentrated projection experiment.

Experiment	Flow $[m^3]$	Depth (1) [cm]	Width [cm]	Height [cm]	Duration [s]	Depth (2) [cm]
1	10	4	40	40	4	4.82
2	10	12	40	40	10	13.57
3	15	6.5	50	50	5	6.56
4	15	–	–	–	6	–
5	15	6.5	48	50	4	6.31
6	20	6.0	50	50	5	7.11
7	20	3.0	36	36	2	2.83

(1) Depth measured with an analogue depth gauge.
(2) Estimated blob depth using measured LiDAR data.

provided. In the case of the square-wave paths, the parameters are the lengths of each horizontal and vertical lines. The paths with ellipses are formed by adding to either the straight or square-wave path, a rotating vector that describes an ellipse with a given frequency and the length of the two ellipse's axes.

The algorithm to generate a path (set of positions) works by taking an initial position and adding a vector to it. The closest 3D point that belongs to the mesh surface (not necessarily a vertex or cell/face centre) is chosen as the next path position and added to a list. Then, the same is done with the latest position added to the list. This is done for one entire section, producing a path as shown in Fig. 6.12a-6.12d. As the path is being generated, the vectors are recalculated so that they follow the mesh curvature. For instance, to create the path shown in Fig. 6.12a, the user only needs to provide an initial position, the distance between targets and the vector that gives the z direction (which is $[0 \quad 0 \quad 1]$ in this example, according to the world reference frame shown in Fig. 6.12 and in Fig. 6.13). For the path shown in Fig. 6.12c, the longitudinal (along axis y) distance between targets and the longitudinal direction are also parameters. As such, two vectors must be updated to make sure the path follows the geometry of the tunnel surface in its cross section and longitudinal axis.

Each target will correspond to a TCP frame, such as the one show in

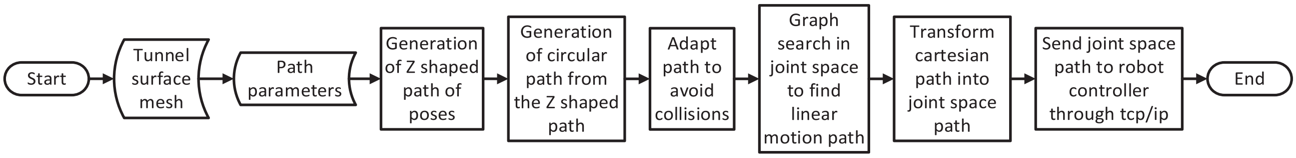

Fig. 6.11. Flowchart of the path generation algorithm.

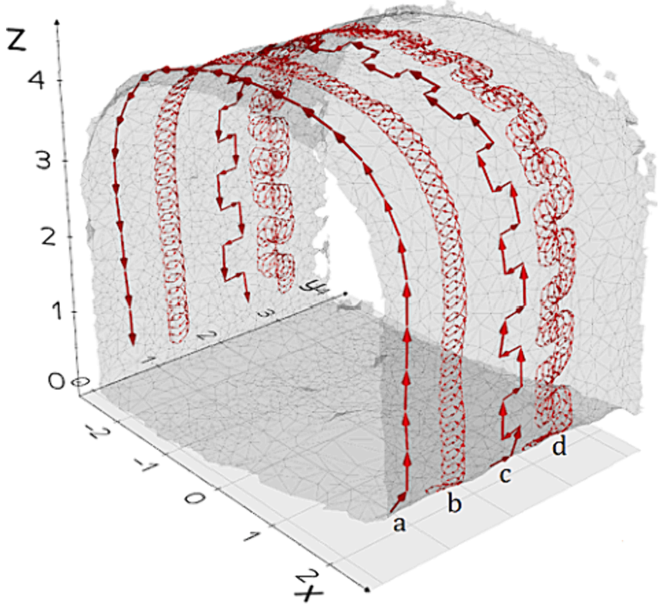

Fig. 6.12. Different types of paths that can be generated. From left to right: a) straight path; b) straight path with ellipses; c) square-wave path; and d) square-wave path with ellipses.

Fig. 6.13, with the algorithm described so far generating the positions for each path target, but not the orientation. The orientation is given by the direction vectors that represent the x, y and z axis of each target pose, as shown in red, green and blue, respectively, in the TCP example in Fig. 6.13. The z vector corresponds to the nozzle projection direction, and should be orthogonal to the mesh to minimize rebound. For each target, the z direction is computed as the average of the normal vectors of the mesh vertices closer to the target position, as shown on Fig. 6.14. The x direction vector must be perpendicular to the z direction vector, resulting in infinite possible solutions (from the point of view of the projection, only the perpendicularly restriction matters). As such, a goal direction is arbitrated as $\begin{bmatrix} 0 & 1 & 0 \end{bmatrix}$ (in world frame coordinates), for the first target, and, for each subsequent target, the goal direction is the one of the previous targets. The actual x direction will be the one that minimizes the x direction change between consecutive targets. Finally, each y direction vector is computed as the normalized cross product of the corresponding z and x direction vectors, to guarantee a direct and orthogonal frame.

6.3.2. *Collision avoidance*

The developed algorithm assumes that the tunnel is free of obstacles, with the FRS robotic arm being supported on a stiff system, rolling on the existing railway of the tunnel to be strengthened. However, one needs to take into consideration the track location, due to possible collisions between the robot and/or the nozzle with the track, as exemplified in Fig. 6.15. These collisions exist given that the path was generated, such that each projection is performed perpendicular to the tunnel surface.

To avoid this problem, each target leading to a collision is reoriented, while maintaining its TCP position (which was already on the tunnel inner surface), so that the robot fist and projection nozzle do not collide with the track. This means that the orthogonality constraint between the projection direction and the mesh will no longer be accomplished, resulting on a slight increase of the rebound, but preventing collisions. Fig. 6.16 shows an example target before (Fig. 6.16a) and after (Fig. 6.16b) the update.

6.3.3. *Search in joint space*

The path must be such that the TCP velocity is constant, and so that the TCP is always perpendicular to the wall, even between targets, which can be (approximately) achieved if a linear motion between consecutive targets (piecewise linear path following) is used. Given the robot positioning with respect to each tunnel section being processed, each cartesian target will result in one or more possible joint configurations, obtained by applying the robot inverse kinematics (each joint configuration is stored as a joint vector, where each vector element corresponds to the robot joint value – articulated robots, such as the one being used here, typically have six joints). However, the robot will only be able to move linearly between consecutive joint targets if these configurations are chosen properly. As such, a graph search is performed in joint space, considering the joint targets corresponding to the cartesian targets previously generated, resulting on a path that is feasible by the robot (for a more detailed description of the search algorithm see (Moniz, 2023).

6.3.4. *Shotcrete simulation*

To assess how layer thickness varies resulting from different paths and different paths' parameters, an algorithm was developed to simulate the shotcrete spraying process. It assumes that, for a given flow and trajectory (TCP) velocity, the concrete projected by the nozzle is distributed according to a paraboloid centred around the attack direction of the nozzle (Chen et al., 2019), with the rebound calculated based on the angle between the mesh surface contact direction, and the normal of the mesh at each point. The simulation also takes into account the concrete flow, which is not constant, but follows a periodic wave

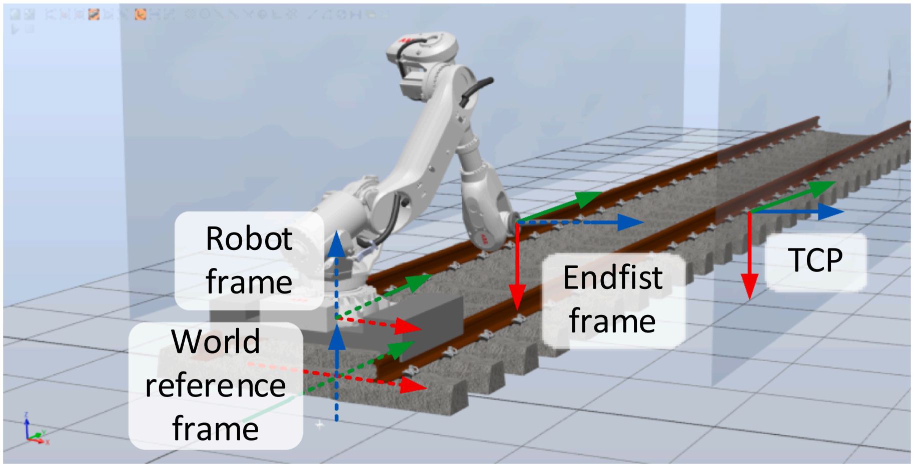

Fig. 6.13. Overview of the used reference frames.

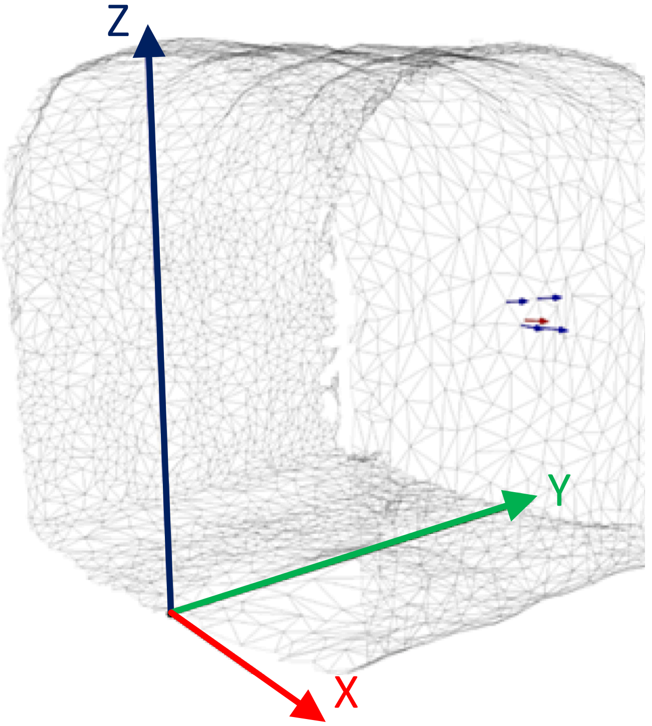

Fig. 6.14. The z direction of a target's orientation (red arrow) is computed as the average of the mesh normal directions near the target's position (blue arrows).

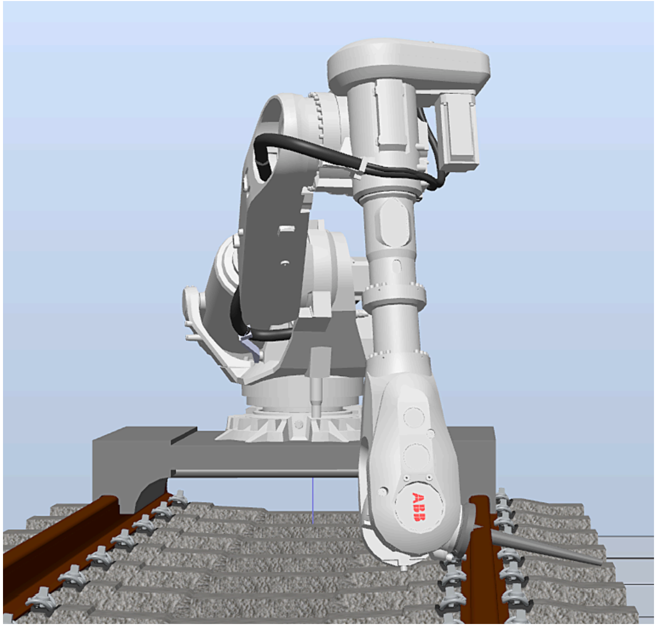

Fig. 6.15. Lower positioned targets may result in the collision of the robot with the tracks.

(Sakoparnig, 2023). As an example of the simulation outcome, the layer resulting from a single straight path with ellipses trajectory is shown in Fig. 6.17. The path shown in Fig. 6.17a is generated using an iterative algorithm and was obtained with non-optimized trajectory parameters, namely a 2.5 cm linear advance per iteration, an angular frequency of 1 rad/iteration, and a 20 cm ellipse radius (for both axis). The shotcrete projection simulation for that path, shown in Fig. 6.17b, was obtained considering a 9.6 m^3 concrete flow, a projection cone with a 50 cm diameter base at 1.5 m projection distance, and a TCP speed of 1.0 m/s. The expected projection result, considering these non-optimized parameters, for the projected area, yielded a layer with an average 1.8 cm thickness, with a maximum thickness of 4.2 cm.

The present focus of this project, regarding the shotcrete automation, is the optimization of the trajectory and motion parameters to ensure that the structural stability project is followed in terms of layer thickness.

6.3.5. Trajectory execution

All the trajectory generation described previously takes place on a computer, which connects through TCP/IP with the robot controller. A specific program was developed to run in the robot controller, which continuously receives sets of targets with the desired speed and motion type. This approach allows the trajectory generation to be done in parallel with the trajectory execution while, at the same time, allowing for the tunnel surface scan to be processed (as described in Section 6.2) and, if needed, a new trajectory be generated from that scan. Given that the targets are sent in batches from the PC to the robot controller, the robot continuously considers the current and the next targets, allowing for a smooth and continuous motion.

7. Conclusions and future work

This paper describes the integrated research activities that are being carried out in the scope of the RoboShot@FRC project for developing a new shotcrete technology capable of applying, in real time, different types of fibre reinforced concrete for the structural rehabilitation of railway tunnels (RT).

Advanced inspection/monitoring systems using laser scanning, photogrammetry and thermography are being adopted to define the geometry and characterize the damages in RT. This information is being integrated with BIM in the context of having the RT's digital twin.

A new computational tool, named by FRMixD, has been developed for the mix design of fibre reinforced concrete/shotcrete (FRC/S), integrating a database with the characteristics of the mixture and corresponding properties at fresh and hardened state. This database is linked to the one existing in the AIpFRC webplatform (aipfrc.org), which integrates machine learning algorithms to assist in proposing the optimum mix composition for FRC/S with target properties at fresh and hardened states.

An extensive experimental program has been carried out with cores, specimens and prototypes of FRS produced in a dedicated tunnel's lab, to determine the properties of FRS at fresh and hardened states, and its classification regarding workability, strength, durability, and toughness, according to existing standards and design codes. Special focus is being done on the characterization of the post-cracking tensile behaviour of FRC, since it is fundamental for the numerical modelling of the FRS shell, up to its collapse, in the context of the structural rehabilitation of a RT.

An integrated design methodology has been used involving two software: $FLAC^{3D}$ for a macro analysis of a tunnel including dedicated constitutive models for soils, capable of simulating the tunnel phase construction and the existing displacement, strain and stress fields, and determine the critical zone in a tunnel for being analysed with a *meso*-model; FEMIX, that has constitutive models capable of simulating the nonlinear behaviour of FRS/C in tension and compression, by simulating the FRS strengthening lining as a layered curved shell, in order for the numerical simulations to be representative of the new robotic-based shotcrete technology. This multiscale modelling strategy was applied to the case study of Mourilhe tunnel, to demonstrate the potential of this shotcrete technology, capable of applying FRS with the required properties for the local being shotcreted, by controlling, in real time, the content of fibres to be added to the shotcreting robot system.

In what concerns the fibre introduction device, the proof-of-concept stage for fibre introduction, dosing and measurements was successfully

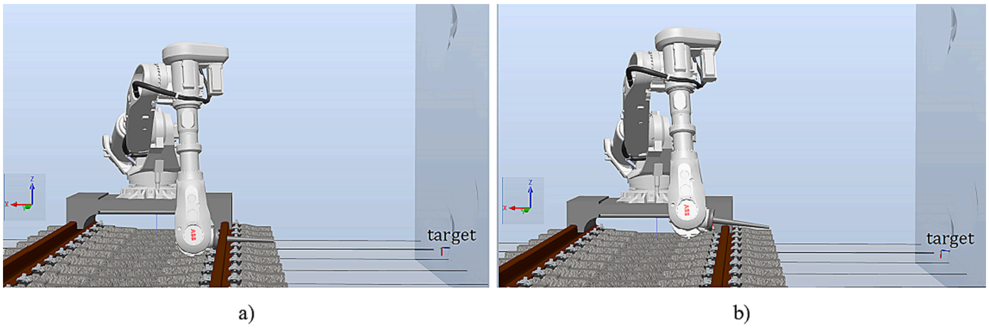

Fig. 6.16. The fist collides with the tracks a), therefore the target's orientation must be updated b).

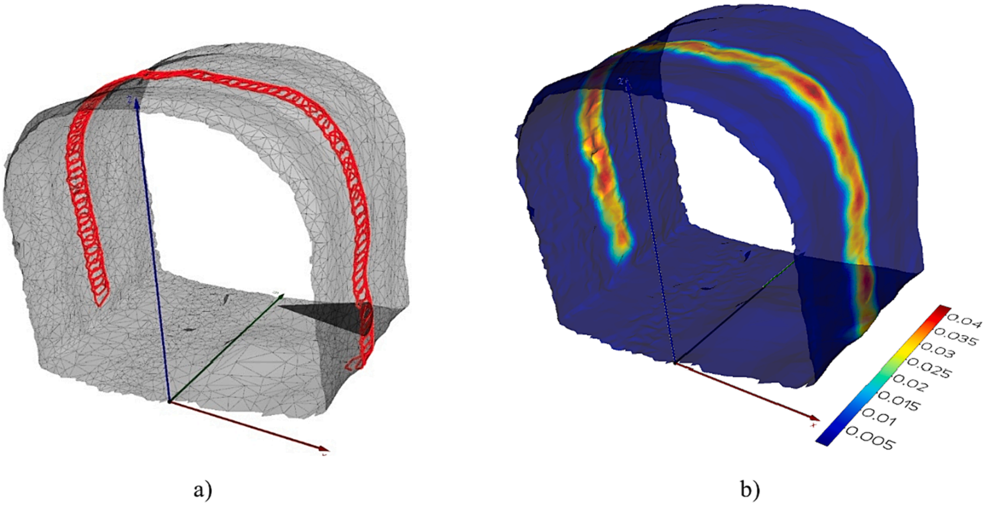

Fig. 6.17. Generated trajectory with the projection cone shown on an example target (a) and, in b), a view of the simulated resulting shotcrete layer, where the colours represent the expected layer thickness in m.

completed, and early initial prototypes were produced, tested, and validated in laboratory environment. At this stage, a design based on a variable volume self-propelled rotary system was proposed for the fibre introduction, allowing for the separation between the high-pressure concrete flow and the atmospheric pressure fibre batch intake, where a fibre feeder arrangement including a motorized belt was designed, prototyped and tested, showing effective prevention of fibre entanglement. A metallic fibre flow rate sensor was also developed and tested. The process of scaling to higher technology readiness levels (TRL 4 and above) is well under way in a close collaboration between academic and industrial partners within the project.

Monitoring the tunnel structure before and after the FRS projection, using LiDAR-based laser scanning and point cloud registration, is crucial to ensure uniform layer thickness, detect imperfections, and apply corrections if needed. The developed system employs SLAM algorithms for automatic alignment of point clouds, using octrees for an efficient representation. The process involves capturing and comparing point clouds using ROS, estimating sensor motion with LiDAR odometry, and registering point clouds to create a global representation of the tunnel surface. The differences between pre- and post-projection point clouds are computed, enabling accurate assessment of FRS depth and surface variations. Future work involves employing more advanced LiDAR sensors for higher precision and resolution, optimizing the registration process, and developing algorithms to detect and correct deviations in real time.

Regarding the automatic trajectory generation and execution, an algorithm was proposed and successfully developed to generate different types of trajectories, given a model of the tunnel surface and desired projection parameters. Tests were successfully performed using a realistic simulator using a typical sized tunnel, as well as using a smaller scale real implementation with an industrial robot in a laboratory environment. Current work is focused on optimizing the trajectory parameters, in order to increase the homogeneity of the projected layer, reducing the projected surface thickness varioation with respect with the structural stability project.

Despite the research methodologies of this project having been applied to RT, they can also be implemented in the rehabilitation of other underground structures with minimal changes whatsoever.

CRediT authorship contribution statement

Joaquim Barros: Conceptualization, Data curation, Formal analysis, Funding acquisition, Investigation, Methodology, Project administration, Resources, Software, Supervision, Validation, Visualization, Writing – original draft, Writing – review & editing. **Hugo Costelha:** Conceptualization, Data curation, Formal analysis, Investigation, Methodology, Software, Supervision, Visualization, Writing – review & editing, Validation. **David Bento:** Formal analysis, Methodology, Resources, Validation, Writing – review & editing. **Nelson Brites:** Conceptualization, Formal analysis, Funding acquisition, Methodology, Supervision, Validation, Writing – review & editing. **Rui Luís:** Formal analysis, Methodology, Resources, Validation, Writing – review & editing. **Hugo Patrício:** Conceptualization, Data curation, Formal analysis, Investigation, Methodology, Software, Supervision, Visualization, Writing – review & editing, Validation. **Vitor Cunha:** Data curation, Formal analysis, Investigation, Supervision, Validation, Writing – review & editing. **Luís Bento:** Formal analysis, Investigation, Supervision, Validation, Writing – review & editing. **Tiago Miranda:** Data curation, Formal analysis, Investigation, Supervision, Writing – review & editing. **Paulo Coelho:** Data curation, Formal analysis, Investigation, Supervision, Writing – review & editing. **Miguel Azenha:** Formal analysis, Investigation, Supervision, Writing – review & editing. **Carlos Neves:** Conceptualization, Formal analysis, Investigation, Methodology, Supervision, Validation, Writing – review & editing. **Hamidreza Salehian:** Investigation, Software, Validation, Writing – review & editing. **Gonçalo Moniz:** Investigation, Software, Validation, Writing – review & editing. **Mojtaba Nematollahi:** Formal analysis, Investigation, Methodology, Software, Validation, Writing – review & editing. **Abel Teixeira:** Formal analysis, Investigation, Software, Validation, Writing – review & editing. **Mahsa Taheri:** Formal analysis, Methodology, Software, Validation, Writing – review & editing. **Anton Mezhyrych:** Formal analysis, Investigation, Software, Validation, Writing – review & editing. **Emad Hosseinpour:** Data curation, Investigation, Validation, Writing – review & editing. **Tales Correia:** Data curation, Investigation, Validation, Writing – review & editing. **Hamid Kazemi:** Data curation, Investigation, Validation, Writing – review & editing. **Omid Hassanshahi:** Data curation, Investigation. **Alireza Rashiddel:** Data curation, Investigation, Validation, Writing – review & editing. **Briar Esmail:** Formal analysis, Investigation.

Declaration of competing interest

The authors declare that they have no known competing financial interests or personal relationships that could have appeared to influence the work reported in this paper.

Data availability

The authors do not have permission to share data.

Acknowledgments

This study is a part of the I&DT project in co-promotion with companies “RoboShot@FRC - Robotized system for the shotcrete of optimized fibre reinforced concrete in railway tunnels”, Co-promotion project number 47075, call 17/SI/2019. This work was partly financed by FCT / MCTES through national funds (PIDDAC) under the R&D Unit Institute for Sustainability and Innovation in Structural Engineering (ISISE), under reference UIDB/04029/2020, under the Associate Laboratory Advanced Production and Intelligent Systems ARISE under reference LA/P/0112/2020, under the R&D Unit INESC Coimbra, Advanced Robotics and Smart Factories (ROBiTECH) group, under reference UIDB/00308/2020, as well as under the Scientific Employment Stimulus - Institutional Call CEECINST/00051/2018. The authors would like to acknowledge the collaboration of Dr. José Granja and the PhD Candidate Mohamad El Sibaii on the development of the example depicted in Fig. 2.2.

References

14:00-17:00, “ISO 19650-1:2018, Organization and digitization of information about buildings and civil engineering works, including building information modelling (BIM) — Information management using building information modelling — Part 1: Concepts and principles,” ISO. Accessed: May 12, 2023. [Online]. Available: https://www.iso.org/standard/68078.html.

2020 buildingSMART, “IFC-Tunnel Project, Report WP2: Requirements analysis report (RAR),” v1.0-2020-07-31. Accessed: May 12, 2023. [Online]. Available: https://publications.cms.bgu.tum.de/reports/IR-TUN_Requirement-Analysis-Report_v1.0.pdf.

Amin, A., Foster, S.J., Muttoni, A., 2015. Derivation of the σ-w relationship for SFRC from prism bending tests. Struct. Concr. 16 (1), 93–105. https://doi.org/10.1002/suco.201400018.

Asteris, P.G., Kolovos, K.G., Douvika, M.G., Roinos, K., Nov. 2016. Prediction of self-compacting concrete strength using artificial neural networks. Eur. J. Environ. Civ. Eng. 20 (sup1), s102–s122. https://doi.org/10.1080/19648189.2016.1246693.

Barros, J.A.O., 2016. Debilities and strengths of FEM-based constitutive models for the material nonlinear analysis of steel fibre reinforced concrete structures. In: Proceedings of the 9th International Conference on Fracture Mechanics of Concrete and Concrete Structures. https://doi.org/10.21012/FC9.023.

Bernard, E.S., Thomas, A.H., 2020. Fibre reinforced sprayed concrete for ground support. Tunn. Undergr. Space Technol. 99, 103302 https://doi.org/10.1016/j.tust.2020.103302.

P.J. Besl, N.D. McKay, Method for registration of 3-D shapes, in Sensor Fusion IV: Control Paradigms and Data Structures, SPIE, Apr. 1992, pp. 586–606. doi: 10.1117/12.57955.

Carvalho, M.R., Barros, J.A.O., Zhang, Y., Dias-da-Costa, D., May 2020. A computational model for simulation of steel fibre reinforced concrete with explicit fibres and cracks. Comput. Methods Appl. Mech. Eng. 363, 112879 https://doi.org/10.1016/j.cma.2020.112879.

W. Chen, X. Wang, H. Liu, Y. Tang, J. Liu, Optimized Combination of Spray Painting Trajectory on 3D Entities, Electronics, vol. 8, no. 1, Art. no. 1, Jan. 2019, doi: 10.3390/electronics8010074.

Cheng, M.-Y., Liang, Y., Wey, C.-M., Chen, J.-C., May 2001. Technological enhancement and creation of a computer-aided construction system for the shotcreting robot. Autom. Constr. 10 (4), 517–526. https://doi.org/10.1016/S0926-5805(00)00104-7.

Chi, Y., Yu, M., Huang, L., Xu, L., Oct. 2017. Finite element modeling of steel-polypropylene hybrid fiber reinforced concrete using modified concrete damaged plasticity. Eng. Struct. 148, 23–35. https://doi.org/10.1016/j.engstruct.2017.06.039.

Chun-Lei, L., Hao, S., Chun-Lai, L., Jin-Yang, L., 2020. Intelligent detection for tunnel shotcrete spray using deep learning and LiDAR. IEEE Access 8, 1755–1766. https://doi.org/10.1109/ACCESS.2019.2962496.

Cunha, V.M.C.F., Barros, J.A.O., Sena-Cruz, J., Apr. 2008. Modelling the influence of age of steel fibre reinforced self-compacting concrete on its compressive behaviour. Mater. Struct. 41 (3), 465–478. https://doi.org/10.1617/s11527-007-9259-4.

Cunha, V.M.C.F., Barros, J.A.O., Sena-Cruz, J.M., Mar. 2012. A finite element model with discrete embedded elements for fibre reinforced composites. Comput. Struct. 94–95, 22–33. https://doi.org/10.1016/j.compstruc.2011.12.005.

V.M.C.F. Cunha, Steel fibre reinforced self-compacting concrete (from micromechanics to composite behavior), doctoral Thesis, 2010. Accessed: May 08, 2023. [Online]. Available: http://repositorium.sdum.uminho.pt/.

Dancygier, A.N., Berkover, E., Mar. 2016. Cracking localization and reduced ductility in fiber-reinforced concrete beams with low reinforcement ratios. Eng. Struct. 111, 411–424. https://doi.org/10.1016/j.engstruct.2015.11.046.

Deluce, J.R., Lee, S.-C., Vecchio, F.J., Jan. 2014. Crack model for steel fiber-reinforced concrete members containing conventional reinforcement. Struct. J. 111 (1), 93–102. https://doi.org/10.14359/51686433.

M. Di Prisco and fib. The International Federation for Structural Concrete, fib Bulletin 105. Fibre Reinforced Concrete. in fib Bulletins. fib. The International Federation for Structural Concrete, 2022. doi: 10.35789/fib.BULL.0105.

A. Edalat Behbahani, J.A.O. Barros, A. Ventura-Gouveia, Plastic-damage smeared crack model to simulate the behaviour of structures made by cement based materials, Int. J. Solids Struct. 73–74 (2015) 20–40, doi: 10.1016/j.ijsolstr.2015.07.027.

Eggert, D., Dalyot, S., 2012. Octree-based SIMD strategy for ICP registration and alignment of 3d point clouds. ISPRS Ann Photogramm. Remote Sens. Spat. Inf. Sci. -3 I–3, 105–110. https://doi.org/10.15488/5192.

C. Eichler, C. Schranz, T. Krischmann, H. Urban, BIMcert Handbook, Basic Knowledge openBIM, 2023rd ed. buildingSMART, 2023. Accessed: May 12, 2023. [Online]. Available: https://www.buildingsmart.co.at/wp-content/uploads/2023/03/BIMcert-Handbook-2023.pdf.

“EN 14488-1:2005 - Testing sprayed concrete - Sampling fresh and hardened concrete.” CEN, Sep. 30, 2005. Accessed: May 12, 2023. [Online]. Available: https://standards.iteh.ai/catalog/standards/cen/c5c14dc2-8945-421a-aa18-d4dba21959e7/en-14488-1-2005.

“EN 14488-3:2006 - Testing sprayed concrete - Part 3: Flexural strengths (first peak, ultimate and residual) of fibre reinforced beam specimens.” CEN. Accessed: May 12, 2023. [Online]. Available: https://standards.iteh.ai/catalog/standards/cen/a7c6a4d3-9ae0-46b4-a764-370b703333d8/en-14488-3-2006.

J. Faury, 1958*Le béton*, 3ème Edition~~. Paris, France: Dunod.

F.P. Figueiredo, J.A.O. Barros, AIpFRC: uma plataforma inteligente para previsões de parâmetros de projeto de estruturas de betão reforçado com fibras, Laboratório Nacional de Engenharia Civil (LNEC), 2022. Accessed: May 08, 2023. [Online]. Available: http://repositorium.sdum.uminho.pt/.

FLAC fast Lagrangian analysis of continua. User’s manual (Version 7.0). Itasca, 2019.

Galan, I., Baldermann, A., Kusterle, W., Dietzel, M., Mittermayr, F., Mar. 2019. Durability of shotcrete for underground support – review and update. Constr. Build. Mater. 202, 465–493. https://doi.org/10.1016/j.conbuildmat.2018.12.151.

Girmscheid, G., Moser, S., May 2001. Fully automated shotcrete robot for rock support. Comput.-Aided Civ Infrastruct. Eng. 16 (3), 200–215. https://doi.org/10.1111/0885-9507.00226.

Han, W., Jiang, Y., Li, N., Wang, G., Luan, H., Liu, C., 2021. Failure behavior and reinforcing design of degraded tunnel linings based on the three-dimensional numerical evaluation. Eng. Fail. Anal. 129, 105677 https://doi.org/10.1016/j.engfailanal.2021.105677.

“HS2 Guide to Tunnelling Costs.” Jun. 11, 2015. Accessed: May 09, 2023. [Online]. Available: https://www.gov.uk/government/publications/hs2-guide-to-tunnelling-costs.

“Infrastructure Cost Review: Technical Report,” HM Treasury, Infrastructure UK, Dec. 2010. Accessed: May 09, 2023. [Online]. Available: https://assets.publishing.service.gov.uk/government/uploads/system/uploads/attachment_data/file/192589/cost_study_technicalnote211210.pdf.

"Inspecção, monitorização e diagnóstico de túneis. Direção de Engenharia da Infra-Estrutura. Estruturas e projetos especiais – Túneis. Inspecção e Diagnóstico." REFER, 2011.

Kargar, A.R., Haghgouei, H., Babanouri, N., Sep. 2020. Time-dependent analysis of stress components around lined tunnels with circular configuration considering tunnel advancing rate effects. Int. J. Rock Mech. Min. Sci. 133, 104422 https://doi.org/10.1016/j.ijrmms.2020.104422.

Kasperkiewicz, J., Racz, J., Dubrawski, A., Oct. 1995. HPC strength prediction using artificial neural network. J. Comput. Civ. Eng. 9 (4), 279–284. https://doi.org/10.1061/(ASCE)0887-3801(1995)9:4(279).

Lai, S., Serra, M., Mar. 1997. Concrete strength prediction by means of neural network. Constr. Build. Mater. 11 (2), 93–98. https://doi.org/10.1016/S0950-0618(97)00007-X.

Lameiras, R., Barros, J.A.O., Azenha, M., May 2015. Influence of casting condition on the anisotropy of the fracture properties of steel fibre reinforced self-compacting concrete (SFRSCC). Cem. Concr. Compos. 59, 60–76. https://doi.org/10.1016/j.cemconcomp.2015.03.008.

Lee, S.-C., Cho, J.-Y., Vecchio, F.J., Sep. 2011. Diverse embedment model for steel fiber-reinforced concrete in tension: model verification. Mater. J. 108 (5), 526–535. https://doi.org/10.14359/51683262.

X. Lin, D. Song, M. Qin, W. Zhang, X. He, B. Xie, An automatic tunnel shotcrete robot, in: 2019 Chinese Automation Congress (CAC), Nov. 2019, pp. 3858–3863. doi: 10.1109/CAC48633.2019.8996350.

Liu, G., Sun, X., Liu, Y., Liu, T., Li, C., Zhang, X., Mar. 2022. Automatic spraying motion planning of a shotcrete manipulator. Intell. Serv. Robot. 15 (1), 115–128. https://doi.org/10.1007/s11370-021-00405-3.

Liu, C., Zhang, D., Zhang, S., 2021. Characteristics and treatment measures of lining damage: a case study on a mountain tunnel. Eng. Fail. Anal. 128, 105595 https://doi.org/10.1016/j.engfailanal.2021.105595.

Lnec, 1993. Concrete - Assessment of the elasticity modulus under uniaxial compression. Laboratório Nacional De Engenharia Civil.

Malagavelli, V., Manalel, P.A., Jul. 2014. Modeling of compressive strength of admixture-based self compacting concrete using fuzzy logic and artificial neural networks. Asian J. Appl. Sci. 7 (7), 536–551. https://doi.org/10.3923/ajaps.2014.536.551.

Malmgren, L., Nordlund, E., Rolund, S., 2005. Adhesion strength and shrinkage of shotcrete. Tunn. Undergr. Space Technol. 20 (1), 33–48. https://doi.org/10.1016/j.tust.2004.05.002.

R. Malva, R. Wißler, The Scanning of Tunnels – The Portuguese Experience, in: Proceedings of the World Tunnel Congress 2014 – Tunnels for a better Life, Foz do Iguaçu, Brazil, May 2014. doi: 10.13140/2.1.4216.6404.

Matos, L.M.P., Barros, J.A.O., Ventura-Gouveia, A., Calçada, R.A.B., Apr. 2021. A new inverse analysis approach for predicting the fracture mode I parameters of fibre reinforced concrete. Eng. Fract. Mech. 246, 107613 https://doi.org/10.1016/j.engfracmech.2021.107613.

L. Medina-Rodríguez, Estudio de los movimientos originados por la excavación de túneles con escudos de presión de tierras en los suelos de Madrid, http://purl.org/dc/dcmitype/Text, Universidade da Coruña, 2000. Accessed: May 08, 2023. [Online]. Available: https://dialnet.unirioja.es/servlet/tesis?codigo=260731.

G. Moniz, H. Costelha, Path Generation and Execution for Automatic Shotcrete in Railway Tunnels, presented at the IEEE International Conference on Autonomous Robot Systems and Competitions (ICARSC), Tomar, Portugal, Apr. 2023, pp. 214–219. doi: 10.1109/ICARSC58346.2023.10129548.

S. Nabulsi, A. Rodriguez, O. Rio, Robotic machine for high-quality shotcreting process, in: ISR 2010 (41st International Symposium on Robotics) and ROBOTIK 2010 (6th German Conference on Robotics), Jun. 2010, pp. 1–8.

Nematollahi, M., Dias, D., Apr. 2019. Three-dimensional numerical simulation of pile-twin tunnels interaction – case of the Shiraz subway line. Tunn. Undergr. Space Technol. 86, 75–88. https://doi.org/10.1016/j.tust.2018.12.002.

Nematollahi, M., Dias, D., Jan. 2020. Interaction between an underground parking and twin tunnels – case of the Shiraz subway line. Tunn. Undergr. Space Technol. 95, 103150 https://doi.org/10.1016/j.tust.2019.103150.

Nunes, S., Pimentel, M., Carvalho, A., Sep. 2016. Non-destructive assessment of fibre content and orientation in UHPFRC layers based on a magnetic method. Cem. Concr. Compos. 72, 66–79. https://doi.org/10.1016/j.cemconcomp.2016.05.024.

Oliver, J., Mora, D.F., Huespe, A.E., Weyler, R., Oct. 2012. A micromorphic model for steel fiber reinforced concrete. Int. J. Solids Struct. 49 (21), 2990–3007. https://doi.org/10.1016/j.ijsolstr.2012.05.032.

Padmarajaiah, S.K., Ramaswamy, A., Apr. 2002. A finite element assessment of flexural strength of prestressed concrete beams with fiber reinforcement. Cem. Concr. Compos. 24 (2), 229–241. https://doi.org/10.1016/S0958-9465(01)00040-3.

M. Quigley et al., ROS: an open-source robot operating system, in: ICRA Workshop on Open Source Software, vol. 3. Jan. 2009.

B. Rail, BIM Knowledge Center. Accessed: May 12, 2023. [Online]. Available: https://www.railbaltica.org/bim-knowledge-center/.

D. Redaelli, A. Muttoni, Tensile Behaviour of reinforced ultra-high performance fiber reinforced concrete elements, in: presented at the fib Symposium, Dubrovnik, 2007, pp. 267–274.

Á. Rodríguez, O. Río, Analysis of real time technical data obtained while shotcreting: An approach towards automation, presented at the ECCOMAS Thematic Conference on Computational Methods in Tunnelling (EURO:TUN 2007), Vienna, Austria, 2007, pp. 156–165.

Rubino, A., Accornero, F., Carpinteri, A., Aug. 2023. Flexural behavior and minimum reinforcement condition in hybrid-reinforced concrete beams. Struct. Concr. 24 (4), 4767–4778. https://doi.org/10.1002/suco.202200674.

Sakoparnig, M., et al., Jan. 2023. On the significance of accelerator enriched layers in wet-mix shotcrete. Tunn. Undergr. Space Technol. 131, 104764 https://doi.org/10.1016/j.tust.2022.104764.

H. Salehian, J.A.O. Barros, Assessment of the performance of steel fibre reinforced self-compacting concrete in elevated slabs, Jan. 2015, doi: 10.1016/j.cemconcomp.2014.09.016.

G.G.S. Sánchez F. A., Comparative study on shotcrete performance in tunnels based on different constitutive approaches, Tunnel. Undergr. Cities. Eng. Innovat. Meet Archaeol. Architecture and Art, CRC Press, 2019.

"Sensors | Free Full-Text | A Novel Approach to Automated 3D Spalling Defects Inspection in Railway Tunnel Linings Using Laser Intensity and Depth Information." Accessed: Nov. 21, 2022. [Online]. Available: https://www.mdpi.com/1424-8220/21/17/5725.

P. Smarzewski, Analysis of failure mechanics in hybrid fibre-reinforced high-performance concrete deep beams with and without openings, Materials 12(1), Art. no. 1, Jan. 2019, doi: 10.3390/ma12010101.

Soltanzadeh, F., Cunha, V.M.C.F., Barros, J.A.O., Dec. 2019. Assessment of different methods for characterization and simulation of post-cracking behavior of self-compacting steel fiber reinforced concrete. Constr. Build. Mater. 227, 116704 https://doi.org/10.1016/j.conbuildmat.2019.116704.

Swaddiwudhipong, S., Seow, P.E.C., Jul. 2006. Modelling of steel fiber-reinforced concrete under multi-axial loads. Cem. Concr. Res. 36 (7), 1354–1361. https://doi.org/10.1016/j.cemconres.2006.03.008.

Taheri, M., Barros, J.A.O., Salehian, H., Ventura-Gouveia, A., Nov. 2022. Numerical assessment of the potential of fibre reinforced shotcrete for structural strengthening of underground masonry tunnels. Tunn. Undergr. Space Technol. 129, 104677 https://doi.org/10.1016/j.tust.2022.104677.

M. Taylor, Crossrail Project: Application of BIM (Building Information Modelling) and Lessons Learned. Accessed: May 12, 2023. [Online]. Available: https://learninglegacy.crossrail.co.uk/documents/crossrail-project-application-of-bim-building-information-modelling-and-lessons-learned/.

Teixeira, M.D.E., Barros, J.A.O., Cunha, V.M.C.F., Moraes-Neto, B.N., Ventura-Gouveia, A., Jan. 2015. Numerical simulation of the punching shear behaviour of self-compacting fibre reinforced flat slabs. Constr. Build. Mater. 74, 25–36. https://doi.org/10.1016/j.conbuildmat.2014.10.003.

Torrents, J.M., Blanco, A., Pujadas, P., Aguado, A., Juan-García, P., Sánchez-Moragues, M.Á., Oct. 2012. Inductive method for assessing the amount and orientation of steel fibers in concrete. Mater. Struct. 45 (10), 1577–1592. https://doi.org/10.1617/s11527-012-9858-6.

J. Walraven, A. Bigaj-van Vliet, fib Model Code for Concrete Structures 2010. Wiley, 2013. Accessed: May 12, 2023. [Online]. Available: https://www.wiley.com/en-us/fib+Model+Code+for+Concrete+Structures+2010-p-9783433604083.

Willam, K.J., Warnke, E.P., 1974. Constitutive model for the triaxial behaviour of concrete in concrete structures subjected to triaxial stresses. IABSE Rep Int. Assoc. Bridge Struct. Eng. 19, 1–30.

Yeh, I.-C., Dec. 1998. Modeling of strength of high-performance concrete using artificial neural networks. Cem. Concr. Res. 28 (12), 1797–1808. https://doi.org/10.1016/S0008-8846(98)00165-3.

Yeh, I.-C., Nov. 1998. Modeling concrete strength with augment-neuron networks. J. Mater. Civ. Eng. 10 (4), 263–268. https://doi.org/10.1061/(ASCE)0899-1561(1998)10:4(263).

Yeh, I.-C., 1999. Design of high-performance concrete mixture using neural networks and nonlinear programming. J. Comput. Civ. Eng. 13 (1), 36–42. https://doi.org/10.1061/(ASCE)0887-3801(1999)13:1(36).

Zhan, Y., Meschke, G., Jul. 2017. Adaptive crack modeling with interface solid elements for plain and fiber reinforced concrete structures. Mater. Basel Switz. 10 (7), 771. https://doi.org/10.3390/ma10070771.

Zhang, D., Zhai, W., Huang, H., Chapman, D., 2019. Robust retrofitting design for rehabilitation of segmental tunnel linings: Using the example of steel plates. Tunn. Undergr. Space Technol. 83, 231–242. https://doi.org/10.1016/j.tust.2018.09.016.

Zhou, M., Cheng, W., Huang, H., Chen, J., 2021. A Novel Approach to Automated 3D Spalling Defects Inspection in Railway Tunnel Linings Using Laser Intensity and Depth Information. Sensors. 21 (17), 5725. https://doi.org/10.3390/s21175725.